

A thermo-optical plane source method to measure thermal conductivity

Cite as: Rev. Sci. Instrum. 96, 074901 (2025); doi: 10.1063/5.0267492

Submitted: 24 February 2025 • Accepted: 4 June 2025 •

Published Online: 2 July 2025



View Online



Export Citation



CrossMark

Jeffrey L. Braun,^{1,a)} Bryan N. Baines,¹ John T. Gaskins,¹ and Patrick E. Hopkins^{1,2,3,4}

AFFILIATIONS

¹ Laser Thermal Analysis, Inc., 937 2nd St. SE, Charlottesville, Virginia 22902, USA

² Department of Mechanical and Aerospace Engineering, University of Virginia, Charlottesville, Virginia 22904, USA

³ Department of Materials Science and Engineering, University of Virginia, Charlottesville, Virginia 22904, USA

⁴ Department of Physics, University of Virginia, Charlottesville, Virginia 22904, USA

^{a)} Author to whom correspondence should be addressed: jeff@laserthermal.com

ABSTRACT

We demonstrate a Thermo-Optical Plane Source (TOPS) technique to measure the thermal conductivity of materials. This high-throughput method measures the thermal conductivity of materials with minimal sample preparation and limited restrictions on sample shape and geometry. Moreover, the technique is applied to solids, liquids, gels, and pastes with no change in implementation. The TOPS technique uses laser heating to induce a steady-state temperature rise in a material and infrared thermography to measure the corresponding temperature rise. Fourier's law is applied to directly measure thermal conductivity, rather than thermal diffusivity or effusivity, eliminating the need for prior knowledge of density and specific heat. We demonstrate the ability to measure thermal conductivities ranging from 0.03 to 60 W m⁻¹ K⁻¹ at room temperature.

© 2025 Author(s). All article content, except where otherwise noted, is licensed under a Creative Commons Attribution-NonCommercial-NoDerivs 4.0 International (CC BY-NC-ND) license (<https://creativecommons.org/licenses/by-nc-nd/4.0/>). <https://doi.org/10.1063/5.0267492>

I. INTRODUCTION

The thermal conductivity (κ) of materials plays a critical role in the design, development, and performance of a wide array of technologies and applications. For example, the efficiency of insulating foams and porous materials for thermal isolation in applications ranging from wearables to building materials is directly tied to their inability to conduct heat.^{1–5} Accurate and high-throughput measurement of these low thermal conductivity materials is an outstanding challenge in this community, where a century old technique, the guarded hot plate method, remains the standard for direct (steady-state) measurements of κ ,⁶ despite a bulky experiment, onerous sample requirements, and measurement times on the order of hours. Another major industry that requires accurate measurements of κ is solid-state energy conversion technologies such as thermoelectric devices,^{7–9} where maintaining a large temperature gradient across materials is paramount and, as such, accurate knowledge of κ for these materials on operational length scales is necessary to evaluate the device performance via the thermoelectric device figure of merit.⁹ On the other end of the spectrum, the higher thermal

conductivities of ceramics, metals, semiconductors, and their composites are a crucial parameter dictating the efficiency of nearly all modern electronic devices,^{10–12} quantifying their ability to dissipate heat generated during operation.

Across a myriad of industries underlying modern technology, accurate measurement of κ can be of utmost importance. The ideal tool for such characterization should be simple to use, relevant to an array of material types, high-throughput, accurate, and repeatable. That is, the ideal technique is capable of measuring κ no matter its value (both low and high extremes), measures various material types and phases (solid, liquid, gels, pastes, gases, powders, etc.) without any change in approach, is nondestructive, is localized to identify differences in thermal properties rather than an aggregate property, is unaffected by sample size or geometry, is unaffected by sample nonidealities such as surface roughness or scratches, and requires little to no sample preparation for measurement. Furthermore, the ideal technique should require minimal assumptions and inputs about the sample; this inherently requires a direct measurement of thermal conductivity rather than a measurement of thermal diffusivity and/or effusivity.

Surveying the field of modern thermal property measurement techniques, although no technique fits this description, significant progress has been made toward this goal. Electrical approaches such as the 3ω technique^{13,14} are able to perform local measurements on a sample from its surface using patterned heaters and thermometers. However, the need to fabricate heaters on the surface presents a high barrier to entry for the technique and significantly limits the types of materials that can be studied. The transient plane source method¹⁵ in its original form suffers from the same limitation regarding patterning, but the hot disk method¹⁶ overcomes this by patterning the metal heater into a polymer layer, which is then sandwiched between two identical samples to be measured. While an improvement in accessibility, it is obviously not ideal to require the fabrication of two identical samples. Moreover, this technique requires specific sample geometries and is an aggregate measurement of thermal diffusivity, not a direct measurement of κ . Furthermore, the contact nature of all electrical techniques is not ideal for many use cases involving *in situ* or quality control testing. While additional testing methods have been validated using the principles of the transient plane source method, allowing for measurements of higher thermal conductivity materials and thin materials and making use of single-sided measurements, they are largely constrained to very specific sample geometries and material property ranges.

Various optical thermometry platforms offer a non-contact alternative and have proven to be viable approaches to measure κ under appropriate operating procedures. Since its inception in the 1960s, Laser Flash Analysis (LFA) has been a ubiquitously utilized method to measure the thermal diffusivity of solids.¹⁷ Traditional implementation of LFA requires a standardized sample geometry and optical access to both the front and back of the specimen for heating and temperature sensing, respectively. In addition, as a dual-sided transient thermometry technique, determining the thermal conductivity requires knowledge of a material's specific heat and density. The advent of laser-based pump-probe thermoreflectance techniques in the 1980s gave rise to new directions for thermal conductivity measurements with much better spatial resolution than laser flash, offering the ability to measure the thermal conductivity of thin films and the thermal conductance across interfaces that were previously inaccessible with LFA.^{18–20} In 2004, a short-pulsed thermoreflectance method, time-domain thermoreflectance (TDTR), became standardized.²¹ This localized measurement uses a focused laser beam rather than a surface flash, giving it superior resolution both spatially and temporally to LFA.²² A similar technique, frequency-domain thermoreflectance (FDTR), simplified the experimental equipment needed by relying on continuous wave lasers to pump and probe a sample.²³ Still, both TDTR and FDTR are transient measurements such that thermal diffusivity or effusivity is fundamentally being measured. More recently, steady-state thermoreflectance (SSTR) was developed, allowing for direct measurement of thermal conductivity with a simple experimental setup.²⁴ Although thermoreflectance techniques are powerful and are unparalleled for thin film measurements,^{25–27} they are not ideal as a general use tool due to their requirements of a mirror finish surface, the necessity of a metal film opto-thermal transducer (requiring an additional tool for deposition), their inability to measure thermal insulators such as foams, and their inability to measure different material phases without significant modification to the experiment.

An alternative approach to thermoreflectance is the use of infrared (IR) thermometry or thermography. Generally referred to as modulated photothermal radiometry (MPTR),^{28,29} various forms of operation exist, but all operate under the same premise: modulate the power of a laser to periodically heat the sample and measure the phase and/or magnitude of the surface temperature response.³⁰ MPTR generally uses a point source measurement of temperature via directing infrared radiation from the area heated by the laser into a detector via a focusing lens or parabolic mirror. A lock-in amplifier is used to capture the temperature phase and/or magnitude at a specific modulation frequency of the pump, and the modulation frequency is varied over a wide range. A thermal model is then used to determine thermal diffusivity by fitting the model to experimental data.³¹ This approach is similar to FDTR but uses a passive IR thermometer as the probe rather than a second laser. An extension of MPTR to thermography³² is often referred to as (laser spot) lock-in thermography^{33–35} or spatially resolved photothermal radiometry.³⁶ In this technique, a modulated laser is focused onto an opaque sample, and a lock-in IR camera captures a thermal image of the surface temperature response, including phase and/or magnitude, at either the front or back of a sample at a specific modulation frequency.³⁷ The laser is generally considered a point source, and the data analysis is based on fitting the relationship between radial distance away from the center of heating and the phase or natural logarithm of the amplitude multiplied by the radial distance at a far enough distance away from the center that the laser beam shape is unimportant and the relationship between these quantities is linear.^{38,39} While losses from convection and radiation can distort this linearity, the model can be adjusted to account for these effects.⁴⁰ Thermal diffusivity is determined from these measurements, from which κ can be derived. When analysis is conducted with temperature magnitude, absolute temperature is not considered; only normalized or relative temperature is considered to avoid the need to know the optical properties of the sample. Thermography has several benefits over the point source MPTR approach, including sampling many pixels for a larger dataset, using the surface image to avoid areas that could negatively affect the measurement, and lock-in thermography, in particular, can overcome the Narcissus effect by filtering noise at all but the modulation frequency. However, a downside is that the diffraction of the infrared radiation when it passes through the lens of the recording camera can affect the readings of the surface temperature. At high frequencies, this generally increases the measured slope of phase vs radius, resulting in thermal diffusivity being overestimated.^{36,41} In addition, the spatially sampled area of the camera is typically much larger than that of a point source pyrometer, leading to lower measurement spatial resolution, typically hundreds of micrometers to millimeters rather than $<100 \mu\text{m}$ achieved in MPTR. Finally, the use of lock-in cameras may be prohibitive in cost and complexity for universal measurements.

To overcome some limitations with lock-in thermography, two alternative thermography approaches have been demonstrated. The first is based on the use of laser pulse heating and recording the resulting surface temperature profile as a function of time.⁴² Whether run in a single sided or dual sided configuration, this technique fundamentally measures thermal diffusivity but has been shown capable of measuring in-plane and cross-plane diffusivity simultaneously for semitransparent materials.⁴³ However, the use of

a pulsed laser increases the cost and complexity of the experiment. More recently, a laser-spot step-heating approach was developed to capture the transient temperature response to continuous wave laser heating.⁴⁴ In this approach, an IR camera is used to record the surface temperature response as a function of time to constant laser heating. Similar to LFA, the relationship between the temperature rise and time is used to extract thermal diffusivity. This represents an improvement in accessibility and ease of use compared to the aforementioned MPTR approaches but still suffers from the same downfalls that prohibit MPTR from being a general use tool: the sample needs to be opaque and highly emissive in the camera's operating wavelength spectrum. This highly limits the types of materials that can be measured. While coatings can be used to overcome this in some cases, it is not universal and can distort the intrinsic thermal properties measured. Moreover, comparing these techniques to lock-in thermography reveals perhaps their biggest limitation: these techniques rely on comparing temperature images (thermograms) frame-to-frame to get a temporal relationship. For entry level infrared cameras, whose accuracy is $\pm 2^\circ\text{C}$, accurate and repeatable data are difficult to obtain. Finally, both of these approaches have largely been limited to measuring the thermal diffusivity of thermal insulators, suggesting their inability to be used as a general purpose technique encompassing a full range of thermal conductivities.

Taken together, we observe the pros and cons of these approaches in order to develop a technique that combines the best of all worlds to get us closer to the ideal κ measurement technique. To this end, we introduce a new technique, Thermo-Optical Plane Source (TOPS), that draws inspiration from both thermoreflectance and infrared thermography techniques. TOPS uses a continuous wave laser to heat a local region of a sample to a steady-state temperature and an entry-level IR camera (without lock-in amplification) to measure the average temperature in the heated region as a function of laser power, the relationship to which Fourier's law is applied to determine thermal conductivity. It is well acknowledged in both the thermoreflectance community and the MPTR community that in order to accurately determine thermal conductivity, one needs to know a material's absorption at the laser wavelength and absolute temperature rise.^{24,45} To overcome this limitation, we

utilize concepts from the thermoreflectance community, specifically SSTR, by incorporating a transducer to allow direct comparison of measurements sample-to-sample via the use of calibration to establish a combined coefficient of emissivity and absorption. Unlike in thermoreflectance, where a metal film is necessary, we use a simple polymer-based film that can be applied to nearly any material, even liquids and gels/pastes. Combining the benefits of a localized and single-sided measurement, resilient to surface roughness and largely independent of sample dimension, we demonstrate a high-throughput, simple, and robust approach that is the closest yet to a universal thermal conductivity measurement technique.

II. PRINCIPLES OF OPERATION

TOPS operates on the principle of Fourier's law; a **continuous heat source with known spatial intensity and power is applied to a local region of the surface of a sample to induce a steady-state temperature rise in the material**. That is, the temperature gradient reaches an equilibrium between the applied heat flux and diffusion into the sample. The time it takes to reach this steady state is dependent on the non-dimensional Fourier number, $\text{Fo} = \alpha t / r_0^2$, where α is the thermal diffusivity, t is the time, and r_0 is the size of the heat source.²⁴ For a $\sim 1\text{ mm}$ diameter source used in this study, a steady-state temperature rise is achieved on the order of 0.1 seconds for high thermal diffusivity materials ($\sim 100\text{ mm}^2/\text{s}$) and on the order of 10 seconds for low thermal diffusivity materials ($\sim 1\text{ mm}^2/\text{s}$). The size of the heat source can be focused for faster measurements at the expense of the spatial resolution of temperature detection. Conversely, the diameter can be expanded for greater spatial resolution and a larger measurement volume. The steady-state temperature rise within the heated region is measured to determine the relationship $\Delta T / \Delta P$, where ΔT is the temperature rise and ΔP is the difference in power of the laser (from off to on state or from power to power if multiple powers are used). $\Delta T / \Delta P$ is then compared to a thermal model to fit the thermal conductivity of the material.

Figure 1 depicts the fundamental concepts on which the TOPS technique operates and the implementation used here. For our heat source, we use a continuous wave laser (Coherent OBIS LX FP

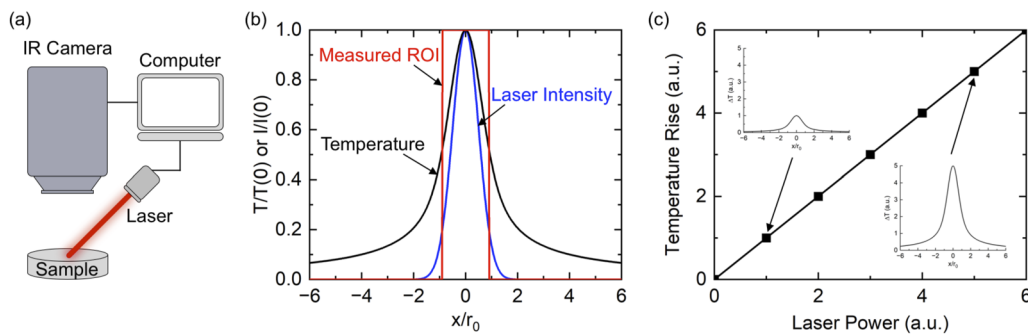


FIG. 1. Concept of the TOPS experiment. (a) Schematic of the experimental setup: a sample is heated by a collimated continuous wave laser at constant power, and the temperature rise is recorded by an infrared camera; a computer is used to automate data collection and synchronize instruments. (b) Normalized intensity of the incident laser on the sample, $I/I(0)$, and resulting temperature rise, $T/T(0)$, as a function of normalized distance from the peak of the intensity (x/r_0 , where r_0 is the $1/e^2$ radius of the laser). The temperature rise is spatially averaged within the Region of Interest (ROI). (c) The ROI steady-state temperature rise vs laser power used to heat the sample: insets show the temperature profile for a low power case and a high power case.

637 nm wavelength) with an available output power from 1 to 120 mW. After collimation, the beam diameter was measured to be 1.08 mm using a beam profiling camera (Gentec-EO Beamage-4M). For temperature measurements, we use an infrared camera (Infratec VarioCAM HDx Head S) with a 30 mm lens to achieve a spatial resolution of about 50 μm per pixel. This uncooled, microbolometer focal plane array camera, operating in the 7.5–14 μm spectral range, is an entry-level camera with no lock-in amplification capability, a relatively slow frame rate of 30 Hz, and a measurement accuracy of $\pm 2^\circ\text{C}$ at room temperature. Nonetheless, we demonstrate a method to negate any inherent noise of the camera in order to achieve accurate thermal measurements. As shown in Fig. 1(a), the laser is directed to the sample and absorbed at the sample surface. The infrared camera measures the surface temperature, and a computer is used to automate the measurement and synchronize the timing. A stage is also used to translate the height of the sample to ensure the laser focus is centered in the infrared camera image for every measurement. Figure 1(b) shows the measurement concept: a Gaussian laser beam is used for heating, resulting in a spatial temperature rise that can be determined by a thermal model.⁴⁶ We define a measurement region of interest (ROI) to spatially average the temperature within that region. The ROI chosen here was a circular region around the center with a diameter of 20 pixels, which equates to where the temperature decay reaches ~50% of its maximum value for a typical sample. For the ~1.1 mm diameter beam used here, this translates to a ~1 mm diameter ROI region. In principle, the choice of ROI is arbitrary, as even a single pixel provides enough information about the temperature rise, but averaging over a larger amount of pixels is preferred to offset fluctuations from noise between individual pixels and reduce the relative impact of outliers. Finally, Fig. 1(c) shows the premise of using multiple laser powers to determine the relationship between this ROI temperature rise and the laser power. With each increasing power, the temperature increases linearly (we limit all temperature rises to a few $^\circ\text{C}$ so thermal properties do not change significantly with temperature), resulting in a $\Delta T/\Delta P$ to which we can fit a thermal model.

In principle, this approach should require the need to know the sample's absorption at the laser wavelength and emissivity in the camera's spectral band. This is possible to obtain with certain materials using complementary techniques such as ellipsometry but is impractical in most cases, restricting measurement to a limited set of materials. In order to generalize this method to all materials, we apply a transducer film to the sample to ensure every measured sample has the same absorption and emissivity, so we can translate a measured $\Delta T/\Delta P$ into a true $\Delta T/\Delta P$. This is akin to common practice in other optical thermal characterization techniques such as laser flash, modulated photothermal radiometry, and thermoreflectance techniques. The transducer layer should be thin enough not to significantly influence the thermal response of the sample but thick enough to completely mask the surface optical properties of the sample. Preferably, this layer should be highly absorbing at the laser wavelength and highly emissive in the camera spectral range. Good candidates for this include thin film carbon, graphite (spray or colloidal suspension), and high emissivity paints. In our case, we use a 5 μm thick film comprised of 2 μm of PET and 3 μm of acrylic adhesive. This transducer proves to be both practical and robust for applying to nearly any type of material, and because it can be suspended over a container, it is ideal for measuring liquids

and gels/pastes. The transducer is used to determine the system proportionality constant that relates the measured data ($\Delta T/\Delta P$)_{measured}, to the true relationship ($\Delta T/\Delta P$). That is

$$\left(\frac{\Delta T}{\Delta P}\right)_{\text{measured}} \propto \frac{\epsilon\tau\Delta T}{\alpha\Delta P} = \gamma\left(\frac{\Delta T}{\Delta P}\right), \quad (1)$$

where ϵ is the transducer emissivity, τ is the transmission of infrared light to the camera (to account for any environmental losses), α is the transducer absorption, and γ is the overall system proportionality constant that can include any other system adjustments unique to a setup (e.g., laser losses from additional optical elements). To determine γ , one can independently determine all the terms that comprise it via other techniques or, more simply, use a calibration sample. In our case, we use a fused silica sample measured with a known thermal conductivity of 1.38 $\text{W m}^{-1} \text{K}^{-1}$.

Once the transducer is applied, a measurement is taken. The goal is to determine the steady-state ROI temperature as a function of laser power to determine $\Delta T/\Delta P$. In practice, we record the temperature as a function of time and average the steady-state temperature over time at each set power. Prior to measurement start, a laser power array, a wait time, and an averaging time are defined. The power array defines the specific powers that will be set during a measurement, the wait time defines the measurement window over which the transient temperature rise will be ignored, and the averaging time defines the time window to average the ROI temperature when the measurement volume has reached a steady-state. When a measurement has started, an automated procedure follows:

1. At each time step, capture a thermogram from the camera.
2. Correct this thermogram in real-time to offset any background or camera drift over time (more on this below).
3. If the time is currently in an averaging window, save the corrected thermogram to a tensor.
4. At the end of the averaging period, take the average of the tensor in the time dimension to obtain an average thermogram representative of the steady-state temperature rise.
5. Extract the ROI temperature from the average thermogram.
6. Repeat steps 1–4 for each power step.
7. Determine $\Delta T/\Delta P$ based on the average ROI temperature vs power relationship.

As a note, the order of operation for data correction and extracting ROI is flexible. To save on computation, one can save the corrected ROI temperature for each time step without creating a tensor of thermograms. However, we find it beneficial to create and save the average thermogram at each power to visualize the temperature image and diagnose any potential concerns during analysis. Figure 2 shows representative measurements taken on a 3-in. diameter fused silica window and demonstrates the concept of data correction we implement for accurate measurement. In general, microbolometer focal plane array based thermal cameras such as the one used here have an absolute temperature accuracy of only $\pm 2^\circ\text{C}$ or $\pm 2\%$, whichever is greater, making them ineffective for determining accurate temperature. However, these cameras can easily have temperature resolution (the ability to distinguish temperature pixel-to-pixel) and sensitivity (responsiveness to change in temperature in time) less than 0.04 $^\circ\text{C}$. This makes them suitable for determining temperature differences. We exploit this principle to correct the

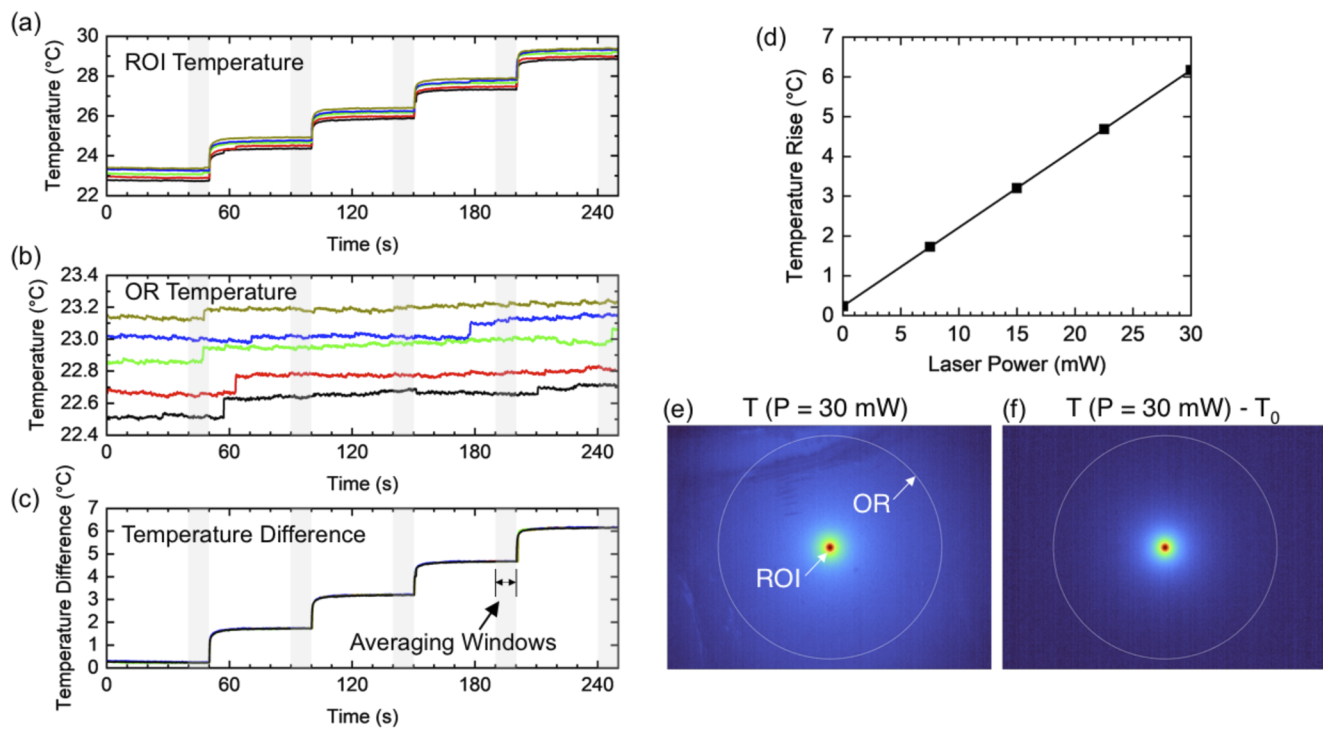


FIG. 2. Measurement data taken on a fused silica sample. (a) Raw temperature data as a function of time for the ROI region of the sample having a 20 pixel, ~ 1 mm diameter and (b) pixels on an outer ring (OR) having a 440 pixel, ~ 22 mm diameter. (c) Temperature difference defined as ROI temperature - OR temperature; this is the processed temperature rise used for analysis. When the temperature is in a steady-state, it is averaged within the defined windows shown as gray bands. (d) The average temperature rises from each averaging window as a function of laser power during that time; the data are shown in symbols, and the best fit line is overlaid. The slope is representative of the sample's thermal conductivity. (e) Thermogram of the sample surface when laser power is set to 30 mW, $T (P = 30 \text{ mW})$, and (f) differential temperature image, $T (P = 30 \text{ mW}) - T_0$, where T_0 is the temperature with no laser heating applied.

ROI temperature in real time by using the difference between the ROI temperature and an outer ring (OR) temperature that is far enough from the heated region to be representative of camera noise rather than laser heating. Figure 2(a) shows the ROI and (b) OR temperatures for five measurements as a function of time. The ROI is defined as an area with a 20 pixel (~ 1 mm) diameter, and the OR is defined as a ring of pixels corresponding to the circle with a 440 pixel (~ 22 mm) diameter. In both cases, the center is that of the peak temperature rise during laser heating, which corresponds to the center of the camera image. The noise in the data, as well as fluctuations in ambient temperature, can make it difficult to obtain consistent quantitative temperatures that can be used for measurement, as evidenced by the spread in temperature shown in Fig. 2(a) and more clearly in Fig. 2(b). Since this noise is common to both ROI and OR temperatures, subtracting the OR from the ROI temperature should offset the noise and leave us with just the temperature rise from laser heating. Figure 2(c) demonstrates that this concept works well for negating such camera noise, where all measurement data appear to converge to the same temperature difference. Moreover, this concept can be applied in real time, frame by frame. Although we use a ring of pixels, this principle can be applied to any quantity representative of the system noise or background drift, including a single pixel; the goal is simply to subtract the representative background noise.

In Figures 2(a)–2(c), averaging windows are shown; these windows allow us to average temporally to further improve the precision of the steady-state ROI temperature at a given laser power. In this case, we average 10 s per power and increase the power from 0 to 30 mW over 5 points. For more thermally conductive samples, the wait and averaging times can be much shorter, typically < 5 s. The resulting relationship is shown in Fig. 2(d), which is the measured steady-state ROI temperature rise vs laser power (which was likewise determined by reading the power of the laser using its internal photodiode at each time step and averaging). The linear relationship is observed, and $\Delta T / \Delta P$ is determined. This is inherently a differential operation, equivalent to subtracting the baseline temperature, i.e., the temperature when the laser is off. An important benefit of using this relationship is that imperfections in surface properties, e.g., scratches or wrinkles in the transducer film, are offset by the differential so that the localized temperature rise from laser heating can be isolated. This can be clearly seen when comparing the raw thermogram in Fig. 2(e), which shows the representative infrared image of the sample when the laser is on at its highest power, and the differential thermogram in Fig. 2(f), which shows the same thermogram subtracted by the thermogram when no laser power is applied. This offset can be helpful for visualization, particularly in real-time during measurement setup, but mathematically makes no

difference in the end result since ΔT is already a differential. Overall, the measurement procedure allows us to take advantage of differential measurements in both time and space to negate the poor absolute temperature accuracy of the camera and instead take advantage of the relatively high sensitivity and resolution, respectively. Once data are collected, we fit a thermal model to the data to extract thermal conductivity. The full details on the temperature rise model are provided in the [supplementary material](#).

III. RESULTS AND DISCUSSION

To demonstrate the capability of TOPS, we measure a wide array of samples ranging in thermal conductivity from 0.03 to $60 \text{ W m}^{-1} \text{ K}^{-1}$, including solids, liquids, and gels/pastes. The latter two categories were tested by applying a suspended layer of the transducer film over a vat that had an input and output port to add a liquid/gel/paste using a syringe; once the vat was full, a valve was closed to contain the sample within the vat, and testing was conducted using the same procedure applied to solid samples. [Table I](#) summarizes the measured values and how they compare with the literature values or, where applicable, what the manufacturer specifies. [Figure 3\(a\)](#) shows the relationship between the

measured and literature/manufacturer values. In general, we see excellent agreement between the literature and measured values. The uncertainty is representative of both spot-to-spot measurement differences (measurement uncertainty) and propagation of uncertainty for parameters in the thermal model (model uncertainty). A full explanation of the uncertainty calculation can be found in the [supplementary material](#). [Figure 3\(b\)](#) shows these uncertainties as a percentage vs the measured κ values determined by TOPS. In general, the spot-to-spot measurement uncertainty is small, typically $<1\%$. On the high end of thermal conductivity ($>30 \text{ W m}^{-1} \text{ K}^{-1}$), the total uncertainty becomes large due to the transducer's thermal resistance. Based on model uncertainty alone, we see that TOPS has a $<5\%$ uncertainty for κ ranging from 0.04 to $20 \text{ W m}^{-1} \text{ K}^{-1}$ and a $<10\%$ uncertainty for κ ranging from 0.018 to $40 \text{ W m}^{-1} \text{ K}^{-1}$. Of course, these uncertainties and limitations are determined based on the specific experimental conditions of our setup. This suggests that adjusting these experimental conditions may allow for extending the measurement range of TOPS. For example, to measure a higher thermal conductivity range with less uncertainty, this may require (1) using a thinner or more thermally conductive transducer or (2) increasing the laser spot size. These concepts are discussed in further detail in the [supplementary material](#), which outlines a path to

TABLE I. Measured thermal conductivities for all samples tested.

Sample	TOPS κ ($\text{W m}^{-1} \text{ K}^{-1}$)	Literature κ ($\text{W m}^{-1} \text{ K}^{-1}$)
Solid samples		
Extruded polystyrene board insulation	0.0295 ± 0.0020	0.030^{a}
NIST SRM 1450e fibrous glass	0.0337 ± 0.0031	0.033^{a} , Ref. 47
Balsa wood	0.0481 ± 0.004	0.0484 , Ref. 48
Acrylic (PMMA)	0.185 ± 0.003	0.19 , Ref. 49
PEEK	0.246 ± 0.004	0.25 , Ref. 50
Borosilicate glass	1.15 ± 0.02	1.15 , Ref. 24
Quartz glass	1.38 ± 0.02	1.38 , Ref. 51
Fused silica	1.38 ± 0.02	1.38 , Ref. 51
Grade 5 titanium (Ti-6Al-4V)	6.80 ± 0.15	6.7 , Ref. 52
CaF ₂ optical window	12.1 ± 0.4	12 , Ref. 53
304 stainless steel	14.9 ± 0.6	14.9 , Ref. 54
Al ₂ O ₃ optical window	33.4 ± 3.0	34 , Ref. 55
Ge optical window	55.7 ± 7.9	60 , Ref. 56
Liquid samples		
Distilled water	0.63 ± 0.014	0.61 , Ref. 57
Propylene glycol	0.197 ± 0.004	0.196 , Ref. 58
Ethylene glycol	0.248 ± 0.005	0.254 , Ref. 59
99% isopropyl alcohol	0.137 ± 0.003	0.137 , Ref. 60
Gel/paste samples		
AOS300	0.98 ± 0.02	0.92^{b} , Ref. 61
AOSXT4	4.1 ± 0.1	5^{b} , Ref. 61
Complex 1381	0.84 ± 0.01	0.75^{b} , Ref. 61
DOW 340	0.69 ± 0.01	0.68^{b} , Ref. 61

^aIndependently measured using a guarded hot plate (ASTM C177).

^bManufacturer specified value.

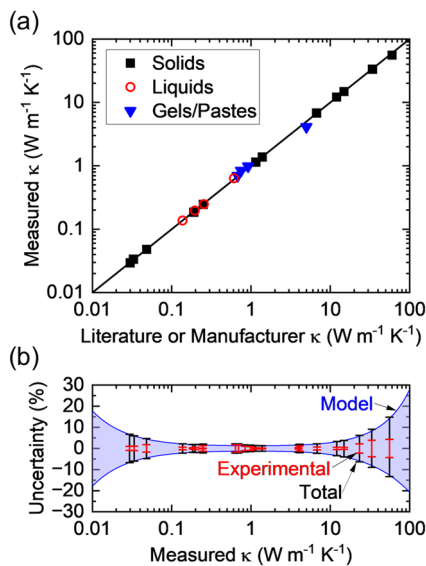


FIG. 3. (a) Measured thermal conductivity vs literature or manufacturer-specified thermal conductivity. Solid samples are depicted in solid squares, liquid samples are depicted in open circles, and gels/pastes are depicted in solid triangles. (b) Uncertainty as a function of measured thermal conductivity: model uncertainty is shown in the blue shaded region, experimental uncertainty is represented by red error bars, and total uncertainty (combining experimental and model) is represented by black error bars.

judiciously tailor these two parameters to maximize sensitivity to a target range of thermal conductivity.

For anisotropic materials, we are fundamentally measuring the geometric mean of thermal conductivity in spherical coordinates.⁶² Thus, for Al_2O_3 and balsa wood, the measured values are compared with their geometric mean counterparts in the literature. For balsa wood and woods in general, which are anisotropic by nature, κ is affected by density, porosity, moisture content, grain direction, and extractive content.⁴⁸ So, the results are expected to be variable by nature, which is what we see in the experiment and is reflected in the measurement uncertainty. Nonetheless, when compared to the average of the range of geometric mean thermal conductivities observed in the literature ($0.0381\text{--}0.0665 \text{ W m}^{-1} \text{ K}^{-1}$),⁴⁸ our measurement of $0.0481 \pm 0.004 \text{ W m}^{-1} \text{ K}^{-1}$ falls in line. Similarly, the NIST SRM 1450e fibrous glass is a material fabricated using layers of discontinuous glass fibers bonded by a thermosetting resin.⁴⁸ While on the macroscale, this layering may induce some minor anisotropy; for our millimeter scale measurement, we do not observe any appreciable contribution to our measurement.

All TOPS measurements were conducted in the open air. When measuring low thermal conductivity materials such as foams, whose thermal conductivities approach that of the air, the impact of the air must be considered as part of the thermal analysis. In fact, air conduction, convection, and even radiation from the surface of the sample have been demonstrated to affect photothermal-based thermal property measurements.^{40,45} Figure 4 shows the relationship between $\Delta T/\Delta P$ and κ . Four thermal models are overlaid to show the effect of the air on the determination of the true thermal conductivity. When air and radiation are not considered at all (the sample

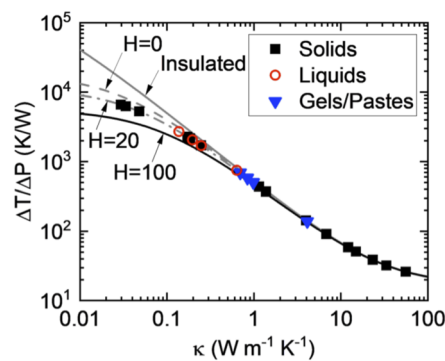


FIG. 4. Effect of air on the experimental results. Measured slope of temperature to power ($\Delta T/\Delta P$) vs thermal conductivity. Solid samples are depicted in solid squares, liquid samples are depicted in open circles, and gels/pastes are depicted in solid triangles. The lines indicate the thermal model with no consideration of air conduction or convection (insulated), only air conduction ($H = 0$), air conduction and $20 \text{ W m}^{-2} \text{ K}^{-1}$ of convection ($H = 20$), and air conduction and $100 \text{ W m}^{-2} \text{ K}^{-1}$ of convection ($H = 100$).

is assumed to be perfectly insulated at the surface), the expected $\Delta T/\Delta P$ matches the experimental data well for materials with a κ of $\sim 0.5 \text{ W m}^{-1} \text{ K}^{-1}$ and higher. However, below this value of κ , the model begins to diverge greatly from the $\Delta T/\Delta P$ we measure experimentally. Hence, one needs to account for air effects on the thermal conductivity, which can be added to the thermal model using a bidirectional boundary condition where heat can flow into the sample and into the air.⁴⁶ Air conduction proves to be the largest contributor to the thermal model, adjusting the thermal model to capture the true thermal conductivities for all but the most insulating samples ($\kappa < 0.1 \text{ W m}^{-1} \text{ K}^{-1}$). We next include the effects of convection as a boundary condition to the surface in the thermal model. A free convection coefficient of room temperature air for moderate temperature rises is on the order of $10 \text{ W m}^{-2} \text{ K}^{-1}$.^{40,45} An additional contribution from radiation can be estimated by $4\sigma T_{\text{amb}}^3$,^{40,45} where σ is the Stephan-Boltzmann constant, to be $\sim 6 \text{ W m}^{-2} \text{ K}^{-1}$ for an ambient temperature, T_{amb} , of 300 K. Thus, a reasonable combined convection coefficient is estimated to be somewhere around $16 \text{ W m}^{-2} \text{ K}^{-1}$. Considering the full set of experimental data, we vary H to determine that a combined coefficient of 20 best captures the data, as shown in Figure 4. Also shown for comparison is the model using a forced convection coefficient of $100 \text{ W m}^{-2} \text{ K}^{-1}$. In this case, the model greatly under-predicts the measured $\Delta T/\Delta P$. While air conduction must always be considered for insulating materials, the effect of convection scales with laser spot size, so one can decrease the size of the laser beam to negate convection effects or increase the size to become more sensitive, opening the door to direct measurement of convection coefficients.

Having established the TOPS technique and validated its ability to measure thermal conductivity, we now push the technique to edge cases in order to assess its limits. To do so, we focus on three case studies: sample thickness dependency, sample edge effects, and surface roughness effects.

First, we consider the case of sample thickness. Similar to other localized thermal characterization methods, TOPS assumes a semi-infinite boundary condition in its analysis; that is, the depth of the

sample is assumed to be infinite in length relative to the heated volume such that heat flux, Q , is 0 at the back of the sample ($Q \rightarrow 0$ as $z \rightarrow \infty$). When the sample becomes thin enough relative to the heat source characteristic length, this assumption breaks down and an adjustment to the model is necessary. We experimentally determine this limit using three sample sets: borosilicate glass, quartz glass, and neoprene rubber (55A hardness). Figure 5 shows the thermal conductivity vs thickness for each set of data. The samples were each tested in two ways: suspended in the air so the backside of the sample was thermally isolated (solid symbols) and placed on an aluminum plate so that heat could flow away from the back of the sample (open symbols).

The borosilicate glass sample set consisted of thicknesses from ~19 mm down to ~3 mm. For all samples in this set that were measured on the aluminum plate, the experimental data had little to no thickness dependence (within uncertainty), indicating that the finite thickness does not affect the thermal model. However, when the sample set was thermally isolated, the 3 mm thick sample showed a minor deviation from the rest of the data, having a 6% reduction on average compared to thicker samples. The quartz glass sample set consisted of thicknesses from ~19 mm down to ~1.6 mm. The same trends as borosilicate can be seen in the quartz glass samples down to 3 mm. At 1.6 mm thickness, the quartz glass sample tested on an aluminum plate was measured as having an increased apparent thermal conductivity compared to that of a bulk sample, while the thermally isolated test measured a significant decrease in apparent thermal conductivity relative to the bulk sample, both well outside of what can be considered uncertainty. The apparent reduction in thermal conductivity is because the sample is suspended in the air, so the thermal penetration depth of the heated volume samples the air, which has a lower thermal conductivity than the quartz glass, reducing the apparent thermal conductivity of the measurement. Conversely, the aluminum stage has the opposite effect, increasing the apparent thermal conductivity of the sample by dissipating heat from the backside more effectively than the sample itself. Finally, we

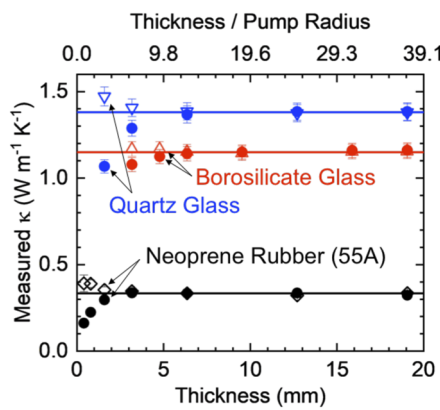


FIG. 5. Effects of thickness on measured thermal conductivity. Solid symbols indicate the measured values on the samples that were thermally isolated during the experiment (suspended in air), while open symbols indicate the measured values on the same samples placed on an aluminum plate during the experiment. Quartz glass, borosilicate glass, and neoprene rubber (55A hardness) are shown. The lines indicate the bulk values as measured on samples with >20 mm thicknesses.

studied a sample set of neoprene rubber, which had thicknesses of ~19 mm down to ~0.4 mm. In this case, we see the same trend as the prior sample sets, remaining constant down to 3 mm thickness. When isolated, at 1.6 mm thickness, the neoprene sample's apparent thermal conductivity is reduced, but smaller in magnitude than the previous cases because the neoprene is more insulating, so the backside air has a relatively smaller effect on the apparent thermal conductivity. For samples having thicknesses of 0.8 and 0.4 mm, we observe a deviation in measured thermal conductivity in both the isolated and non-isolated cases compared to the thicker samples. The isolated samples show a reduced apparent thermal conductivity, consistent with the two prior sample sets, while the non-isolated sample shows a higher apparent thermal conductivity due to the aluminum plate having a significantly higher thermal conductivity. As a note, the quality of the contact between the 0.4 mm sample and the aluminum plate dictates the thermal interface resistance between the sample and this plate. In the 0.4 mm thick sample, we observed significant measurement uncertainty from spot-to-spot measurements due to the sample's uneven contact with the plate when only being pressed down by its own weight. A more robust heat sinking method may greatly enhance the increase in apparent thermal conductivity with decreasing sample thickness.

Previous work on the depth-dependent temperature decay reveals that the $1/e$ temperature decay in depth occurs at approximately the $1/e^2$ Gaussian radius of the laser heating event.⁴⁶ Although this $1/e$ decay is conventionally referred to as the thermal penetration depth, this term is misleading in that the temperature profile extends well beyond this length, and thus any modifications of the sample beyond this length (e.g., finite thickness or boundary) can still affect the temperature at the surface. The analytical solution of the temperature decay is asymptotic toward 0 as depth into the sample approaches infinity. Practically, however, there is a depth at which the temperature has decayed enough that it does not affect the surface temperature. For thermally isolated samples, experimental data suggest the thickness should be at least 4 \times the beam diameter. Placing the sample on a conductive heat sink helps provide a means to drive this requirement to ~2–3 \times . Despite these limitations of using the semi-infinite model, it is possible to modify the model to account for a finite thickness by applying a backside boundary condition.⁴⁰

Next, we consider the effect of lateral sample dimension on the measurement, specifically the effect of breaking the radial symmetry of the temperature profile by approaching the edge of a sample. We conducted measurements on two samples: 304 stainless steel and acrylic, both of which are circular samples with a 50 mm diameter and 12.5 mm thickness. The measurement consists of adjusting the position of the laser beam center away from the edge of the sample in discrete points; exact distances from the edge were determined using the infrared image to count the pixels between the center of the heated region and the sample edge. Figure 6 shows the results of this study. For both samples, a reduction in measured thermal conductivity is observed as the distance to the edge approaches 0. This effect can be explained by the fact that heat is confined in one lateral dimension, which means one path for heat dissipation has been restricted; the result is a higher temperature within the region of interest, thus reducing the apparent thermal conductivity in that area. This effect occurs between 1 and 1.5 mm for acrylic and is more pronounced in 304 stainless steel, occurring around 2 mm from the

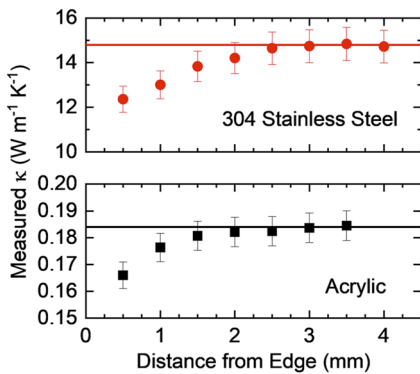


FIG. 6. Effect of the sample edge on a measurement: Measured thermal conductivity (top) of 304 stainless steel and (bottom) of acrylic vs distance of the center of the heated region from the edge. The symbols indicate the measured data, and the solid lines represent the thermal conductivity near the center of the sample, at least 20 mm from the edge.

edge. Note that the first point (0.5 mm) from the edge is the closest the laser can physically get to the edge without clipping the sample edge. In fact, taking a measurement with the beam at the 0 position, where half the beam is clipping the sample edge, resulted in an increased κ almost twice the bulk κ due to the fact that only half the power was being absorbed by the sample.

This case study shows that such a deviation between edge κ and bulk κ may initially be viewed as a limitation of TOPS, but it highlights a major advantage of TOPS in its capability to resolve *local* κ . That is, the measured κ is representative of the effective κ near the edge of a sample, where this confinement effect would have real implications on a device dissipating heat. As a comparison, traditional lock-in and step thermography techniques rely on fitting a model of temperature rise vs distance from the heated center region out to several multiples of the beam radius away from

the center to derive the bulk κ . In contrast, TOPS relies on a local measurement of the temperature within about $2\times$ the beam diameter. As such, TOPS is far better suited for non-uniform samples with various surface defects that would otherwise distort the temperature profile globally but not locally. Combined with the differential nature of the measurement, TOPS proves to be highly robust for localized thermal measurements.

Finally, we consider the effect of surface roughness on the measurement. To do so, we study four materials ranging three orders of magnitude in thermal conductivity: 304 stainless steel, grade 5 titanium, quartz glass, and acrylic. Surface roughening was performed on each set of these materials using aluminum oxide sand blasting. The surface roughness was varied by exposing the sample to sand blasting for incrementally longer periods of time. The roughness was then quantified using mechanical profilometry to obtain an average root mean square (RMS) roughness and standard deviation from three scans on each sample. We find that this surface roughening procedure had varying impacts on the different materials. Quartz glass showed the most significant roughness range, having an upper average RMS roughness near $10\ \mu\text{m}$. The other three materials were not able to be roughened nearly as much, having a maximum average RMS roughness of about $2.5\ \mu\text{m}$ for acrylic, $2.3\ \mu\text{m}$ for stainless steel, and $1.6\ \mu\text{m}$ for titanium.

Figure 7 summarizes the results of this study. Beginning with 304 stainless steel, Fig. 7(a) shows the measured thermal conductivity vs average RMS roughness to reveal two distinct regions of data: a constant measured κ with roughness and a linearly decreasing measured κ with roughness. A polished control sample was included in the study for reference to highlight when this transition becomes significant enough to deviate from experimental uncertainty; the shaded region shows the error band for the control sample thermal conductivity. In order to determine the cutoff roughness where deviation occurs, we fit a piecewise linear function to the data (represented by the line going through the data) to capture both distinct regions and use the transition point to indicate the cutoff

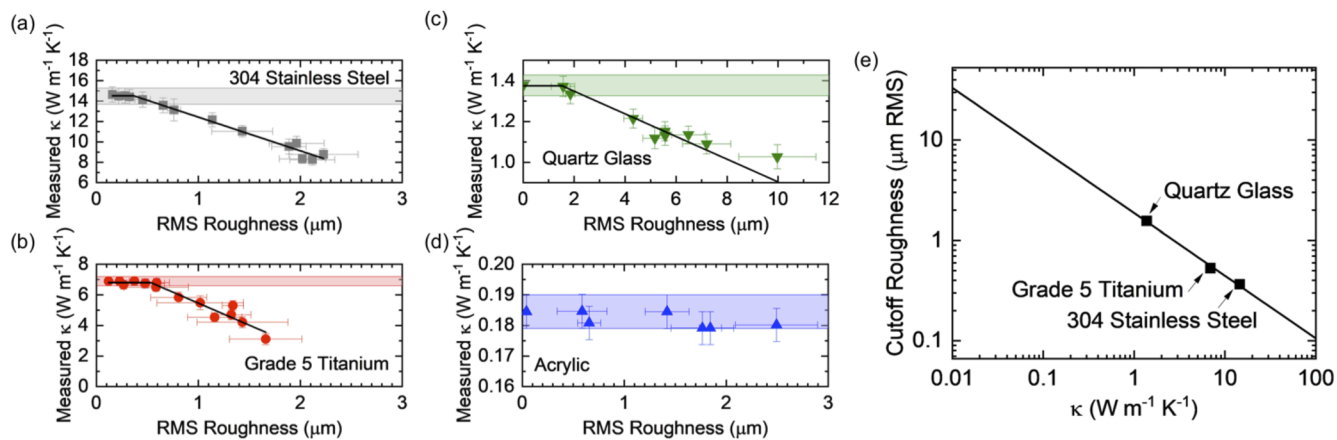


FIG. 7. Effects of roughness on measured thermal conductivity: Measured κ vs average RMS roughness for (a) 304 stainless steel, (b) grade 5 titanium, (c) quartz glass, and (d) acrylic. The symbols and error bars indicate the experimental data, and the shaded region represents the thermal conductivity bounds (including the total uncertainty range) of the control sample. The lines represent a piecewise linear fit to the data to characterize the distinct regions of (1) constant κ with increasing roughness and (2) decreasing κ with increasing roughness. (e) Relationship between cutoff roughness and κ . The symbols show the measured data, and the line shows a best-fit logarithmic function.

RMS roughness. This exact procedure is repeated for (b) grade 5 titanium and (c) quartz glass to obtain a cutoff average RMS roughness. As shown in Fig. 7(d) for acrylic, we were not able to obtain a cutoff because the average RMS roughness could not be increased enough to measure any significant reduction in thermal conductivity. Nonetheless, with the data we have from stainless steel, titanium, and quartz glass, we can establish an empirical relationship between the cutoff average RMS roughness and the sample thermal conductivity. Figure 7(e) shows this relationship, which proves to be a logarithmic function as shown by the best fit line displayed. With the caveat that the dataset is limited to just three data points and, thus, limits confidence in extrapolation, it is nonetheless instructive to apply this function to the extremes to assess the potential limits to TOPS. On the low-end of κ , very rough samples can be measured without loss of accuracy. This explains why we were not able to roughen acrylic enough to measure a reduction in κ ; we would need to roughen it to an RMS roughness of more than $5\ \mu\text{m}$ to begin to measure any reduction. On the high end of the κ range, relatively smooth samples are necessary for measurement. An average RMS roughness of 100 nm or less is needed for a material with a thermal conductivity of $100\ \text{W m}^{-1}\ \text{K}^{-1}$. From a practical perspective, obtaining such roughness levels is obtainable via mechanical polishing techniques for most materials. In the experimental data presented in Table I, all samples had roughness levels well below the cutoff roughness threshold estimated using this rule of thumb, such that roughness was not a concern.

Assessing the physical reason for this roughness dependency, we first note that TOPS is an optical technique relying on heating via laser absorption and temperature measurement via infrared thermography, both of which can be affected by surface roughness. The surface emissivity can increase with roughness,⁶³ which would result in a higher apparent temperature rise for the same applied laser power. Similarly, increased surface roughness can lead to increased laser absorption,⁶⁴ again leading to a higher temperature rise for the same applied laser power. Both of these would lead to a reduced apparent thermal conductivity. However, these would require the transducer layer to match the surface roughness of the sample when applied, perfectly fitting into the peaks and valleys of the sample surface. In reality, air gaps form between the transducer and sample such that the transducer is, on average, smoother than the sample. Moreover, if emissivity and absorption were the culprits, the cut-off RMS roughness would be the same for all materials. Instead, we attribute the reason for the reduction in measured κ with increasing roughness to an increasing thermal interface resistance between the transducer and sample due to the aforementioned imperfect contact at the interface. When this thermal interface resistance becomes large enough, the assumed thermal model does not properly capture this effect by default, leading to a reduced apparent thermal conductivity.

IV. SUMMARY

In conclusion, in this paper, we have demonstrated a Thermo-Optical Plane Source (TOPS) technique for thermal conductivity measurements. Using laser heating to induce a localized steady-state temperature rise at the surface of a sample that is detected using infrared thermography, the relationship between power and temperature is used to directly measure a material's thermal conductivity

without any knowledge of heat capacity or density. We demonstrate a frame-by-frame spatial temperature correction and temporal differential measurement approach to make highly accurate thermal measurements with an entry-level IR camera, effectively improving accuracy by two orders of magnitude compared to the intrinsic temperature accuracy of the camera. We use this approach to measure the thermal conductivity of solid, liquid, and gel/paste samples ranging from 0.03 to $60\ \text{W m}^{-1}\ \text{K}^{-1}$, accounting for environmental effects to ensure measurements can be done in the open air, even for highly insulating materials. Furthermore, we show the robustness of the technique by demonstrating it is insensitive to sample thickness down to $2\text{-}3\times$ the laser beam diameter and highly resilient to sample roughness. Altogether, TOPS offers a universal approach for simple, accurate, and high-throughput thermal conductivity measurements.

SUPPLEMENTARY MATERIAL

The [supplementary material](#) is included to provide details on the following: a derivation of the thermal model used to determine thermal conductivity, sample preparation, ways to potentially increase the measurement range via transducer selection, and uncertainty analysis.

ACKNOWLEDGMENTS

This work was funded in part by the Office of Naval Research, Grant No. N00014-23-1-2630.

AUTHOR DECLARATIONS

Conflict of Interest

The authors are all employees of Laser Thermal, a company that manufactures and sells commercial thermal conductivity measurement tools.

Author Contributions

Jeffrey L. Braun: Conceptualization (lead); Data curation (lead); Formal analysis (lead); Investigation (lead); Methodology (lead); Writing – original draft (lead). **Bryan N. Baines:** Data curation (equal); Investigation (supporting); Methodology (supporting); Writing – review & editing (supporting). **John T. Gaskins:** Conceptualization (supporting); Investigation (supporting); Methodology (supporting); Writing – review & editing (supporting). **Patrick E. Hopkins:** Conceptualization (supporting); Investigation (supporting); Methodology (supporting); Writing – review & editing (supporting).

DATA AVAILABILITY

The data that support the findings of this study are available from the corresponding author upon reasonable request.

REFERENCES

- Z. Qin, M. Li, J. Flohn, and Y. Hu, "Thermal management materials for energy-efficient and sustainable future buildings," *Chem. Commun.* **57**(92), 12236–12253 (2021).

- ²A. Pasupathy, R. Velraj, and R. V. Seeniraj, "Phase change material-based building architecture for thermal management in residential and commercial establishments," *Renewable Sustainable Energy Rev.* **12**(1), 39–64 (2008).
- ³Z. Ma, D. Zhao, C. She, Y. Yang, and R. Yang, "Personal thermal management techniques for thermal comfort and building energy saving," *Mater. Today Phys.* **20**, 100465 (2021).
- ⁴Y. Jung, M. Kim, T. Kim, J. Ahn, J. Lee, and S. H. Ko, "Functional materials and innovative strategies for wearable thermal management applications," *Nano-Micro Lett.* **15**(1), 160 (2023).
- ⁵Y. S. Ju, "Thermal management and control of wearable devices," *iScience* **25**(7), 104587 (2022).
- ⁶ASTM C177-13: Standard Test Method for Steady-State Heat Flux Measurements and Thermal Transmission Properties by Means of the Guarded-Hot-Plate Apparatus.
- ⁷L. Li, W.-D. Liu, Q. Liu, and Z.-G. Chen, "Multifunctional wearable thermoelectrics for personal thermal management," *Adv. Funct. Mater.* **32**(22), 2200548 (2022).
- ⁸H. A. Eivari, Z. Sohbatzadeh, P. Mele, and M. H. N. Assadi, "Low thermal conductivity: Fundamentals and theoretical aspects in thermoelectric applications," *Mater. Today Energy* **21**, 100744 (2021).
- ⁹M. Zebarjadi, K. Esfarjani, M. S. Dresselhaus, Z. F. Ren, and G. Chen, "Perspectives on thermoelectrics: From fundamentals to device applications," *Energy Environ. Sci.* **5**(1), 5147–5162 (2012).
- ¹⁰E. Pop, "Energy dissipation and transport in nanoscale devices," *Nano Res.* **3**, 147–169 (2010).
- ¹¹R. J. Warzoha, A. A. Wilson, B. F. Donovan, N. Donmezler, A. Giri, P. E. Hopkins, S. Choi, D. Pahinkar, J. Shi, S. Graham, Z. Tian, and L. Ruppalt, "Applications and impacts of nanoscale thermal transport in electronics packaging," *J. Electron. Packag.* **143**, 020804 (2021).
- ¹²J. Mathew and K. Shankar, "A review on transient thermal management of electronic devices," *J. Electron. Packag.* **144**, 010801 (2021).
- ¹³S.-M. Lee and D. G. Cahill, "Heat transport in thin dielectric films," *J. Appl. Phys.* **81**, 2590 (1997).
- ¹⁴C. Dames, "Measuring the thermal conductivity of thin films: 3 omega and related electrothermal methods," *Annu. Rev. Heat Transfer* **16**, 7 (2013).
- ¹⁵S. E. Gustafsson, "Transient plane source techniques for thermal conductivity and thermal diffusivity measurements of solid materials," *Rev. Sci. Instrum.* **62**(3), 797–804 (1991).
- ¹⁶M. Gustavsson, E. Karawacki, and S. E. Gustafsson, "Thermal conductivity, thermal diffusivity, and specific heat of thin samples from transient measurements with hot disk sensors," *Rev. Sci. Instrum.* **65**(12), 3856–3859 (1994).
- ¹⁷ASTM E1461-13: Standard Test Method for Thermal Diffusivity by the Flash Method.
- ¹⁸J. Opsal, A. Rosencwaig, and D. L. Willenborg, "Thermal-wave detection and thin-film thickness measurements with laser beam deflection," *Appl. Opt.* **22**(20), 3169–3176 (1983).
- ¹⁹A. Rosencwaig, J. Opsal, W. L. Smith, and D. L. Willenborg, "Detection of thermal waves through optical reflectance," *Appl. Phys. Lett.* **46**(11), 1013–1015 (1985).
- ²⁰C. A. Paddock and G. L. Eesley, "Transient thermoreflectance from thin metal films," *J. Appl. Phys.* **60**(1), 285–290 (1986).
- ²¹D. G. Cahill, "Analysis of heat flow in layered structures for time-domain thermoreflectance," *Rev. Sci. Instrum.* **75**, 5119 (2004).
- ²²D. H. Olson, J. L. Braun, and P. E. Hopkins, "Spatially resolved thermoreflectance techniques for thermal conductivity measurements from the nanoscale to the mesoscale," *J. Appl. Phys.* **126**(15), 150901 (2019).
- ²³A. J. Schmidt, R. Cheaito, and M. Chiesa, "A frequency-domain thermoreflectance method for the characterization of thermal properties," *Rev. Sci. Instrum.* **80**(9), 094901 (2009).
- ²⁴J. L. Braun, D. H. Olson, J. T. Gaskins, and P. E. Hopkins, "A steady-state thermoreflectance method to measure thermal conductivity," *Rev. Sci. Instrum.* **90**(2), 024905 (2019).
- ²⁵D. H. Olson, C. M. Rost, J. T. Gaskins, C. J. Szwejkowski, J. L. Braun, and P. E. Hopkins, "Size effects on the cross-plane thermal conductivity of transparent conducting indium tin oxide and fluorine tin oxide thin films," *IEEE Trans. Compon., Packag., Manuf. Technol.* **9**(1), 51–57 (2019).
- ²⁶P. Jiang, X. Qian, and R. Yang, "Tutorial: Time-domain thermoreflectance (TDTR) for thermal property characterization of bulk and thin film materials," *J. Appl. Phys.* **124**(16), 161103 (2018).
- ²⁷A. J. Schmidt, "Pump-probe thermoreflectance," *Annu. Rev. Heat Transfer* **16**, 159 (2013).
- ²⁸P.-E. Nordal and S. O. Kanstad, "Photothermal radiometry," *Phys. Scr.* **20**(5–6), 659 (1979).
- ²⁹R. Santos and L. C. M. Miranda, "Theory of the photothermal radiometry with solids," *J. Appl. Phys.* **52**(6), 4194–4198 (1981).
- ³⁰J. Corona and N. Kandadai, "Recent progress in modulated photothermal radiometry," *Sensors* **23**(10), 4935 (2023).
- ³¹S. Pham Tu Quoc, G. Cheymol, and A. Semerok, "New contactless method for thermal diffusivity measurements using modulated photothermal radiometry," *Rev. Sci. Instrum.* **85**(5), 054903 (2014).
- ³²F. Cernuschi, P. G. Bison, A. Figari, S. Marinetti, and E. Grinzato, "Thermal diffusivity measurements by photothermal and thermographic techniques," *Int. J. Thermophys.* **25**(2), 439–457 (2004).
- ³³A. Salazar, A. Mendioroz, R. Fuente, and R. Celorio, "Accurate measurements of the thermal diffusivity of thin filaments by lock-in thermography," *J. Appl. Phys.* **107**(4), 043508 (2010).
- ³⁴A. Bedoya, E. Marín, J. J. Puldón, and C. García-Segundo, "On the thermal characterization of insulating solids using laser-spot thermography in a front detection configuration," *Int. J. Thermophys.* **44**(2), 27 (2022).
- ³⁵A. U. Gaitonde, A. A. Candadai, J. A. Weibel, and A. M. Marconnet, "A laser-based Ångstrom method for in-plane thermal characterization of isotropic and anisotropic materials using infrared imaging," *Rev. Sci. Instrum.* **94**(7), 074904 (2023).
- ³⁶S. Paoloni and D. Fournier, "Spectral dependence of signal distortions in spatially resolved photothermal radiometry," *J. Appl. Phys.* **92**(10), 5950–5954 (2002).
- ³⁷R. Fuente Dacal, *Thermal and Optical Characterization of Heterogeneous Materials by Infrared Lock-In Thermography* (Universidad del País Vasco-Euskal Herriko Unibertsitatea, 2012), <http://purl.org/dc/dcmitype/Text>.
- ³⁸L. Fabbri and P. Fenici, "Three-dimensional photothermal radiometry for the determination of the thermal diffusivity of solids," *Rev. Sci. Instrum.* **66**(6), 3593–3600 (1995).
- ³⁹A. Mendioroz, R. Fuente-Dacal, E. Apiñaniz, and A. Salazar, "Thermal diffusivity measurements of thin plates and filaments using lock-in thermography," *Rev. Sci. Instrum.* **80**(7), 074904 (2009).
- ⁴⁰A. Salazar, A. Mendioroz, and R. Fuente, "The strong influence of heat losses on the accurate measurement of thermal diffusivity using lock-in thermography," *Appl. Phys. Lett.* **95**(12), 121905 (2009).
- ⁴¹J. F. Bisson and D. Fournier, "Influence of diffraction on low thermal diffusivity measurements with infrared photothermal microscopy," *J. Appl. Phys.* **83**(2), 1036–1042 (1998).
- ⁴²I. Philipp, J. C. Batsale, D. Maillet, and A. Degiovanni, "Measurement of thermal diffusivities through processing of infrared images," *Rev. Sci. Instrum.* **66**(1), 182–192 (1995).
- ⁴³N. W. Pech-May, A. Mendioroz, and A. Salazar, "Simultaneous measurement of the in-plane and in-depth thermal diffusivity of solids using pulsed infrared thermography with focused illumination," *NDT E Int.* **77**, 28–34 (2016).
- ⁴⁴A. Salazar, M. Colom, and A. Mendioroz, "Laser-spot step-heating thermography to measure the thermal diffusivity of solids," *Int. J. Therm. Sci.* **170**, 107124 (2021).
- ⁴⁵A. Salazar, A. Mendioroz, F. Rodríguez-Valdés, A. Bedoya, E. Marín, and C. García-Segundo, "Strong influence of the surrounding gas in laser-spot lock-in thermography," *J. Appl. Phys.* **133**(18), 185104 (2023).
- ⁴⁶J. L. Braun and P. E. Hopkins, "Upper limit to the thermal penetration depth during modulated heating of multilayer thin films with pulsed and continuous wave lasers: A numerical study," *J. Appl. Phys.* **121**(17), 175107 (2017).

- ⁴⁷R. R. Zarr and N. Alan Heckert, "Certification of Standard Reference Material 1450e fibrous glass board," Technical Report No. NIST SP 260-201, National Institute of Standards and Technology, Gaithersburg, MD, April 2020.
- ⁴⁸N. J. Kotlarewski, B. Ozarska, and B. K. Gusamo, "Thermal conductivity of Papua New Guinea Balsa wood measured using the needle probe procedure," *BioResources* **9** (2014).
- ⁴⁹M. J. Assael, S. Botsios, K. Gialou, and I. N. Metaxa, "Thermal conductivity of polymethyl methacrylate (PMMA) and borosilicate crown glass BK7," *Int. J. Thermophys.* **26**(5), 1595–1605 (2005).
- ⁵⁰See <https://www.mcam.com/en/products/peek> for "PEEK plastics."
- ⁵¹See <https://www.corning.com/worldwide/en/products/advanced-optics/product-materials/semiconductor-laser-optic-components/high-purity-fused-silica.html> for information about High Purity Fused Silica from Corning.
- ⁵²G. Welsch, R. Boyer, and E. W. Collings, *Materials Properties Handbook: Titanium Alloys* (ASM International, 1993).
- ⁵³G. A. Slack, "Thermal conductivity of CaF₂, MnF₂, CoF₂, and ZnF₂ crystals," *Phys. Rev.* **122**(5), 1451–1464 (1961).
- ⁵⁴R. H. Bogaard, "Thermal conductivity of selected stainless steels," in *Thermal Conductivity 18*, edited by T. Ashworth and D. R. Smith (Springer, Boston, MA, 1985), pp. 175–185.
- ⁵⁵R. B. Wilson and D. G. Cahill, "Limits to Fourier theory in high thermal conductivity single crystals," *Appl. Phys. Lett.* **107**(20), 203112 (2015).
- ⁵⁶C. J. Glassbrenner and G. A. Slack, "Thermal conductivity of silicon and germanium from 3 K to the melting point," *Phys. Rev.* **134**(4A), A1058–A1069 (1964).
- ⁵⁷M. L. V. Ramires, C. A. Nieto de Castro, Y. Nagasaka, A. Nagashima, M. J. Assael, and W. A. Wakeham, "Standard reference data for the thermal conductivity of water," *J. Phys. Chem. Ref. Data* **24**(3), 1377–1381 (1995).
- ⁵⁸T. Sun and A. S. Teja, "Density, viscosity and thermal conductivity of aqueous solutions of propylene glycol, dipropylene glycol, and tripropylene glycol between 290 K and 460 K," *J. Chem. Eng. Data* **49**(5), 1311–1317 (2004).
- ⁵⁹M. Afrand, "Experimental study on thermal conductivity of ethylene glycol containing hybrid nano-additives and development of a new correlation," *Appl. Therm. Eng.* **110**, 1111–1119 (2017).
- ⁶⁰See <https://thermtest.com/application/thermal-conductivity-solvents> for "Testing the Thermal Conductivity of Solvents."
- ⁶¹See <https://www.mcmaster.com/> for the McMaster-Carr catalog.
- ⁶²J. L. Braun, C. J. Szwejkowski, A. Giri, and P. E. Hopkins, "On the steady-state temperature rise during laser heating of multilayer thin films in optical pump-probe techniques," *J. Heat Transfer* **140**(5), 052801 (2018).
- ⁶³Z. Zhang, M. Chen, L. Zhang, H. Li, H. Huang, Z. Zhang, P. Yu, Y. Niu, S. Gao, C. Wang, and J. Jiang, "A straightforward spectral emissivity estimating method based on constructing random rough surfaces," *Light: Sci. Appl.* **12**(1), 266 (2023).
- ⁶⁴V. Gareyan and Z. Gevorkian, "Impact of surface roughness on light absorption," *Phys. Rev. A* **109**(1), 013515 (2024).

A Thermo-Optical Plane Source Method to Measure Thermal Conductivity: Supplementary Material

Jeffrey L. Braun,* Bryan N. Baines, and John T. Gaskins
Laser Thermal Analysis, Inc., 937 2nd St SE, Charlottesville, VA 22902 USA

Patrick E. Hopkins
Laser Thermal Analysis, Inc., 937 2nd St SE, Charlottesville, VA 22902 USA
Department of Mechanical and Aerospace Engineering,
University of Virginia, Charlottesville, Virginia 22904, USA
Department of Materials Science and Engineering,
University of Virginia, Charlottesville, Virginia 22904, USA and
Department of Physics, University of Virginia, Charlottesville, Virginia 22904, USA

* jeff@laserthermal.com

I. TEMPERATURE RISE MODEL

The heat diffusion equation in cylindrical coordinates is

$$\kappa_z \left\{ \frac{1}{r} \frac{\partial T(z, r, t)}{\partial r} + \frac{\partial^2 T(z, r, t)}{\partial r^2} \right\} + \kappa_z \frac{\partial^2 T(z, r, t)}{\partial z^2} = \rho c_p \frac{\partial T(z, r, t)}{\partial t}, \quad (\text{S1})$$

where κ_r and κ_z are in-plane and cross-plane thermal conductivity, respectively, T is the temperature (relative to some initial temperature) at a given spatial and time combination, r denotes the radial coordinate variable, z denotes the cross-plane coordinate variable orthogonal to r , ρ is the mass density, c_p is the specific heat capacity, and t is the time variable. The typical TOPS sample stack is shown in Fig. S1; a transducer is applied to the sample and air is in contact with the transducer. The laser heats the top of the transducer surface. As such, the boundary conditions are given by

$$T(0, r, t) = T_{\text{top}}(r, t) \quad (\text{S2})$$

$$\frac{\partial T(z, r, t)}{\partial z} \Big|_{z=0} = -\frac{1}{\kappa_z} Q_{\text{top}}(r, t), \quad (\text{S3})$$

where the $T_{\text{top}}(r, t)$ and $Q_{\text{top}}(r, t)$ are the temperature and heat flux at the top surface of a given material. $Q_{\text{top}}(r, t)$ is the net heat flux at the sample surface

$$Q_{\text{top}}(r, t) = -Q_{\text{air, conduction}}(r, t) - HT_{\text{top}}(r, t) + Q_{\text{laser}}(r, t), \quad (\text{S4})$$

where $Q_{\text{air, conduction}}$ is the heat conduction (including Kapitza conductance) to air, H is the effective convection coefficient that includes the sum of the air convection coefficient and the linearized radiation coefficient. Q_{laser} is the heat provided by the laser to the sample surface, defined by

$$Q_{\text{laser}} = \frac{2}{\pi r_0^2} \exp \left(-\frac{2r^2}{r_0^2} \right) G(t), \quad (\text{S5})$$

where r_0 is the $1/e^2$ radius of the laser at the sample surface and $G(t)$ defines the time variation of the laser; in our case, this is constant but the solution is generalized so that any function (e.g. with amplitude modulation at a specific frequency or pulsed laser) can be used. Taking the Fourier transform ($t \rightarrow \omega$) and Hankel transform ($r \rightarrow k$) simplifies Eq. S1 to

$$\frac{\partial^2 \tilde{T}(z)}{\partial z^2} = q^2 \tilde{T}(z). \quad (\text{S6})$$

The notation used here is such that for a function $Y(z, r, t)$, \tilde{Y} denotes the Fourier transform of Y , and $\tilde{\tilde{Y}}$ denotes the Hankel transform of \tilde{Y} . q is defined as

$$q^2 = \frac{\kappa_r k^2 + i \rho c_p \omega}{\kappa_z}. \quad (\text{S7})$$

The transformed heat flux on the top surface from Eq. S4 becomes

$$\tilde{Q}_{\text{top}} = -\tilde{Q}_{\text{air, conduction}}(k, \omega) - H \tilde{T}_{\text{top}}(k, \omega) + \tilde{Q}_{\text{laser}}(k, \omega), \quad (\text{S8})$$

where

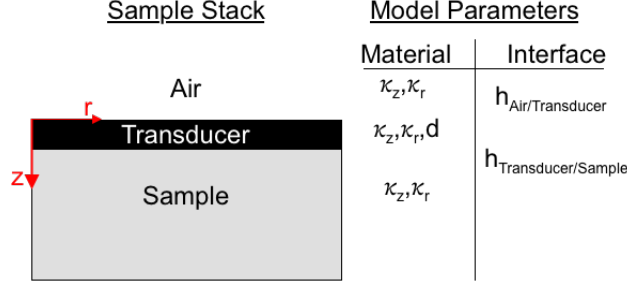


FIG. S1. Schematic of sample stack: the material layers modeled include air, the transducer, and sample. The thermal model includes cross-plane thermal conductivity (κ_z) in-plane thermal conductivity (κ_z) for each layer as well as the thickness of the transducer layer (d) and the interface conductances between air and transducer ($h_{\text{Air/Transducer}}$) and between the transducer and sample ($h_{\text{Transducer/Sample}}$).

$$\tilde{Q}_{\text{laser}}(k, \omega) = \frac{1}{2\pi} \exp\left(\frac{-k^2 r_0^2}{8}\right) G(\omega), \quad (\text{S9})$$

Within any layer of the material stack, the temperature and heat flux at any given depth, z , can be related to the top temprature of the material by the following:

$$\begin{bmatrix} \tilde{T}(z, k, \omega) \\ \tilde{Q}(z, k, \omega) \end{bmatrix} = \begin{bmatrix} \cosh(qz) & -\frac{1}{q\kappa_z} \sinh(qz) \\ -q\kappa_z \sinh(qz) & \cosh(qz) \end{bmatrix} \begin{bmatrix} \tilde{T}_{\text{top}}(k, \omega) \\ \tilde{Q}_{\text{top}}(k, \omega) \end{bmatrix}. \quad (\text{S10})$$

Likewise, at the bottom of each layer, the thermal boundary conductance between the layers (e.g. between layer $n-1$ and n) needs to be considered. The relationship between temperature and heat flux at the bottom of layer $n-1$ and the top of layer n is given by:

$$\begin{bmatrix} \tilde{T}_{\text{bot},n-1} \\ \tilde{Q}_{\text{bot},n-1} \end{bmatrix} = \begin{bmatrix} 1 & -\frac{1}{h_{n-1,n}} \\ 0 & 1 \end{bmatrix} \begin{bmatrix} \tilde{T}_{\text{top},n} \\ \tilde{Q}_{\text{top},n} \end{bmatrix}, \quad (\text{S11})$$

where $h_{n-1,n}$ is the thermal boundary conductance between layer $n-1$ and layer n . When considering multiple layers, one can apply a matrix method, also known as the thermal quadrupole method, to get

$$\begin{bmatrix} \tilde{T}_{\text{bot}} \\ \tilde{Q}_{\text{bot}} \end{bmatrix} = \prod_{i=n, n-1, \dots}^{i=1} \mathbf{M}_i \mathbf{N}_i \begin{bmatrix} \tilde{T}_{\text{top}} \\ \tilde{Q}_{\text{top}} \end{bmatrix} = \begin{bmatrix} \tilde{A}(k, \omega) & \tilde{B}(k, \omega) \\ \tilde{C}(k, \omega) & \tilde{D}(k, \omega) \end{bmatrix} \begin{bmatrix} \tilde{T}_{\text{top}} \\ \tilde{Q}_{\text{top}} \end{bmatrix} \quad (\text{S12})$$

$$\mathbf{M}_i = \begin{bmatrix} \cosh(q_i L_i) & -\frac{1}{q_i \kappa_z} \sinh(q_i L_i) \\ -q_i \kappa_z \sinh(q_i L_i) & \cosh(q_i L_i) \end{bmatrix} \quad (\text{S13})$$

$$\mathbf{N}_i = \begin{bmatrix} 1 & -\frac{f(i)}{h_{i-1,i}} \\ 0 & 1 \end{bmatrix} \quad (\text{S14})$$

$$f(i) = \begin{cases} 1 & i \neq 1 \\ 0 & i = 1 \end{cases} \quad (\text{S15})$$

$$q_i^2 = \frac{1}{\kappa_{z,i}}(i\omega\rho_i c_{p,i} + \kappa_{r,i} k^2). \quad (\text{S16})$$

For this generalized solution, \tilde{T}_{top} is determined by invoking a semi-infinite boundary condition for bulk samples so that $\lim_{z \rightarrow \infty} \tilde{Q}_n(z, k, \omega) = 0$, such that

$$\tilde{T}_{\text{top}} = - \left(\frac{\tilde{D}}{\tilde{C}} \right)_{\text{sample}} \tilde{Q}_{\text{top}}. \quad (\text{S17})$$

Likewise, the air conduction can also be defined based on the air side properties through the same means to get

$$\tilde{Q}_{\text{air,conduction}} = \left(\frac{\tilde{D}}{\tilde{C}} \right)_{\text{air}}^{-1} \tilde{T}_{\text{top}}, \quad (\text{S18})$$

where the $\left(\frac{\tilde{D}}{\tilde{C}} \right)_{\text{air}}$ term for air includes the air properties and also the thermal boundary conductance (Kapitza conductance) between the surface and the air. The term is positive because z is defined to be positive in the direction of the sample, so the air goes to $-z$; as such, to invoke Eq. S12, a sign reversal of $\tilde{B}(k, \omega)$ and $\tilde{C}(k, \omega)$ is necessary since $\sinh(z)$ is an odd function. Combining Eq. S8 and Eq. S17, \tilde{T}_{top} is

$$\tilde{T}_{\text{top}} = - \left(\frac{\tilde{D}}{\tilde{C}} \right)_{\text{sample}} [\tilde{Q}_{\text{air,conduction}} - H \tilde{T}_{\text{top}} + \tilde{Q}_{\text{laser}}]. \quad (\text{S19})$$

Substituting in Eq. S18 leads to

$$\tilde{T}_{\text{top}} = - \left(\frac{\tilde{D}}{\tilde{C}} \right)_{\text{sample}} \left[\left(\frac{\tilde{D}}{\tilde{C}} \right)_{\text{air}}^{-1} \tilde{T}_{\text{top}} - H \tilde{T}_{\text{top}} + \tilde{Q}_{\text{laser}} \right]. \quad (\text{S20})$$

Solving for \tilde{T}_{top} yields

$$\tilde{T}_{\text{top}} = \frac{- \left(\frac{\tilde{D}}{\tilde{C}} \right)_{\text{sample}} \tilde{Q}_{\text{laser}}}{\left[1 + \left(\frac{\tilde{D}}{\tilde{C}} \right)_{\text{sample}} \left(\frac{\tilde{D}}{\tilde{C}} \right)_{\text{air}}^{-1} - H \left(\frac{\tilde{D}}{\tilde{C}} \right)_{\text{sample}} \right]}. \quad (\text{S21})$$

We can define the transfer function as $Z(k, \omega)$ to simplify the relationship to

$$\tilde{T}_{\text{top}}(k, \omega) = Z(k, \omega) \tilde{Q}_{\text{laser}}(k, \omega). \quad (\text{S22})$$

This solution is still defined in the Hankel and frequency domains. To go back to radial coordinates, the inverse Hankel transform is taken to get the temperature rise needed to compare with experimental data.

$$T_{\text{top}}(r, \omega) = \int_0^\infty Z(k, \omega) \tilde{Q}_{\text{laser}}(k, \omega) J_0(kr) k dk. \quad (\text{S23})$$

In the steady-state, we set $\omega = 0$ Hz to comply with the constant power condition, but the same equation can be applied when ω is nonzero. This defines the temperature profile radially.

In the standard TOPS measurement, we take an average temperature within a region of interest (ROI). To determine this average temperature, mathematically we can integrate the temperature from 0 to the ROI radius, r_1 . Or, we can integrate from 0 to ∞ after convoluting with the heaviside step function having an on state when $r \leq r_1$ and off when $r > r_1$, where r_1 is the radius defining the ROI, and dividing by the area. The temperature rise in the ROI region would then be

$$T_{\text{ROI}}(\omega) = \frac{1}{\pi r_1^2} \int_0^{r_1} T_{\text{top}}(r, \omega) 2\pi r \, dr = \frac{1}{\pi r_1^2} \int_0^{\infty} T_{\text{top}}(r, \omega) h(r_1 - r) 2\pi r \, dr, \quad (\text{S24})$$

where $h(r_1 - r)$ is the heaviside step function. Substituting Eq. S23 into Eq. S24 yields

$$\begin{aligned} T_{\text{ROI}}(\omega) &= \frac{1}{\pi r_1^2} \int_0^{\infty} \left[\int_0^{\infty} Z(k, \omega) \tilde{Q}_{\text{laser}}(k, \omega) J_0(kr) k \, dk \right] h(r_1 - r) 2\pi r \, dr \\ &= \frac{2}{r_1^2} \int_0^{\infty} Z(k, \omega) \tilde{Q}_{\text{laser}}(k, \omega) \left[\int_0^{\infty} h(r_1 - r) J_0(kr) r \, dr \right] k \, dk \\ &= \frac{2}{r_1^2} \int_0^{\infty} Z(k, \omega) \tilde{Q}_{\text{laser}}(k, \omega) \left[\frac{r_1}{k} J_1(r_1 k) \right] k \, dk \\ &= \frac{2}{r_1} \int_0^{\infty} Z(k, \omega) \tilde{Q}_{\text{laser}}(k, \omega) J_1(r_1 k) \, dk. \end{aligned} \quad (\text{S25})$$

where J_1 is the Bessel function of first kind of order 1. Finally, expanding the laser heating term by substituting in Eq. S9 gives

$$\begin{aligned} T_{\text{ROI}}(\omega) &= \frac{2}{r_1} \int_0^{\infty} Z(k, \omega) \left[\frac{1}{2\pi} \exp\left(\frac{-k^2 r_0^2}{8}\right) G(\omega) \right] J_1(r_1 k) \, dk \\ &= \frac{G(\omega)}{\pi r_1} \int_0^{\infty} Z(k, \omega) \exp\left(\frac{-k^2 r_0^2}{8}\right) J_1(r_1 k) \, dk. \end{aligned} \quad (\text{S26})$$

In all modeling done in this paper, we use the following model inputs: The air layer has $\kappa = 0.026 \text{ Wm}^{-1}\text{K}^{-1}$ and infinite thickness, the transducer layer has a thickness of $5 \mu\text{m}$ and $\kappa \approx 0.294 \text{ Wm}^{-1}\text{K}^{-1}$ (determined by TOPS measurement when run on a silicon window), and the sample of interest layer has an assumed infinite thickness, and the thermal conductivity is fit for. In all cases, heat capacity is not needed in the steady-state; the modulation frequency ω is set to 0 in Eq. S26. A thermal boundary conductance (Kapitza conductance) is assumed to be $1 \text{ MW/m}^2\text{-K}$ between air and the transducer, and $10 \text{ MW/m}^2\text{-K}$ between the transducer and sample. Both of these boundary conductances were chosen to be arbitrarily high while being realistic values; the idea is that the experiment operates in a regime in which we are insensitive to the interface resistance. On the air side, the air is so insulating that it is unrealistic for the thermal boundary conductance to play a role in contributing to the total thermal resistance. On the sample side, consider that the transducer alone has a thermal resistance of $d/\kappa \approx 1.7 \times 10^{-5} \text{ m}^2\text{K W}^{-1}$ (a conductance of $\sim 5.9 \times 10^4 \text{ Wm}^{-2}\text{K}^{-1}$). Based on sensitivity arguments discussed below, the sample thermal resistance for any material less than $30 \text{ Wm}^{-1}\text{K}^{-1}$ will be greater than that of the transducer, often by orders of magnitude due to scaling with thermal conductivity. So, in order for the thermal interface resistance to have a significant effect on the model, it would have to be on the same level as these two resistances. We determined in Fig. 7 that this is possible under the right conditions and that the assumption of a negligible thermal interface resistance does break down when the thermal interface conductance becomes low enough due to surface roughness. So it is important that the sample surface comply to the rule of thumb determined by Fig. 7(c) in its surface roughness. That is, average RMS surface roughness should satisfy the relation: $\log(\delta_{\text{RMS}}) < -0.616 \log(\kappa) + 0.279$, where δ_{RMS} is the RMS roughness in microns and κ is in $\text{Wm}^{-1}\text{K}^{-1}$.

II. SAMPLE PREPARATION

For solid samples, there is minimal sample preparation involved. The transducer film is simply applied to the sample by adhering it to the surface of the sample and spreading it to reduce any wrinkles or air gaps as much possible. Fig. S2 shows an example of a sample (a) without a transducer and (b) with a transducer applied. Because of the localized nature of the measurement, it is only important that the measurement area (i.e. the area on the surface that

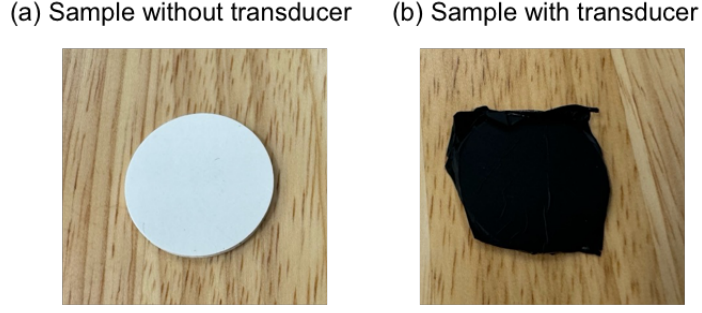


FIG. S2. Example of sample (a) without transducer and (b) with transducer applied.

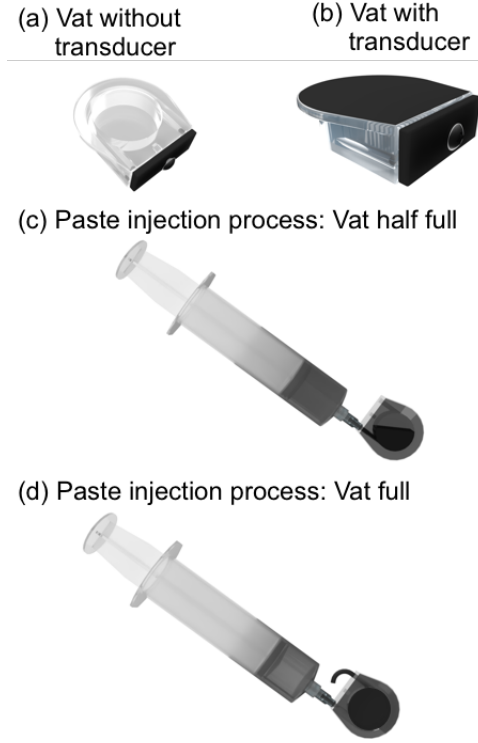


FIG. S3. Rendering of sample preparation process for gel and paste samples. (a) Vat shown without a transducer applied. (b) Vat shown with a transducer applied. (c) Injection of sample into vat, shown when the vat is half filled. (d) Injection of sample into vat when vat is full; note that the sample begins to overflow out of the overflow port.

the laser is heating) be in good contact with the surface. As such, we find that even with a poorly applied transducer, there are typically many good measurement areas on the sample still. We use the thermal image of the surface to identify such areas and avoid any wrinkles; even with no laser heating it is generally obvious which areas to avoid.

To measure gels and pastes, we use a 3D printed vat having an opening of 5 mm depth by 10 mm diameter to hold the paste when it is injected. A rendering of this vat is shown in Fig. S3(a). Two holes are included through the back wall of the vat to provide an injection port and overflow port; the injection port is closer to the top of the sample. We place the transducer on the empty vat to form a seal at the top of the vat, shown in Fig. S3(b). We then inject the sample into the injection hole with the vat upside down and at an angle; this ensures the sample fills completely to make contact with the transducer before coming out of the overflow hole when full. This process is shown in Fig. S3(c) and (d) for when the vat is half filled and full, respectively. For gels and pastes that are stiff enough to hold their shape, we simply cover the two holes with a 3D-printed wall that plugs the two holes in the wall and proceed with the TOPS measurement. For liquids and samples that do not hold their shape, we instead attach

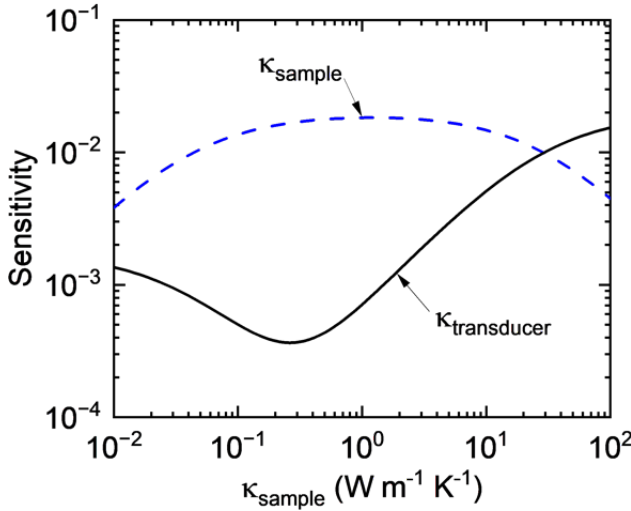


FIG. S4. Sensitivity to thermal conductivity of the sample (κ_{sample}) and the transducer ($\kappa_{\text{transducer}}$) as a function of sample thermal conductivity (κ_{sample}).

a tube to the injection and overflow ports of the vat. We inject the liquid in a similar way, but when overflowing, we close the valves on both sides when the vat is full. By filling the vat at an angle, we can ensure any trapped air bubbles are contained in the overflow port tube rather than the sample surface.

III. TRANSDUCER SELECTION AND EFFECTS ON THERMAL MODEL

The choice of transducer for TOPS is a balancing act between ensuring sufficient optical absorption of the laser together with appropriate emissivity in the operating band of the infrared camera and having a minimal thermal resistance so that only the sample's thermal resistance dictates the temperature rise induced by laser heating. To understand the influence of the transducer on the thermal model, we can conduct a sensitivity analysis, where we perturb a variable in the model to quantify its relative influence on the model. We define sensitivity as[2]

$$S_x = \frac{|\Delta T_{x+\Delta} - \Delta T_{x-\Delta}|}{\Delta T_x}, \quad (\text{S27})$$

where x is the model variable being perturbed and Δ is the perturbation amount, the actual quantity of which is unimportant since S_x is only a relative quantity to other variables and we assume no nonlinear property behavior for small perturbations. For simplicity, we define the perturbation to be 1%. Since we are ultimately interested in measuring thermal conductivity, we can plot sensitivity of the thermal conductivity of the sample and the transducer layer together vs. the thermal conductivity of the sample, shown in Fig.S4.

Using our experimental conditions, we can compare the sensitivity to the sample's thermal conductivity (κ_{sample}) and the transducer's thermal conductivity ($\kappa_{\text{transducer}}$) as a function of κ_{sample} . Fig. S4 reveals that the model is overwhelmingly sensitive to κ_{sample} up to about $30 \text{ Wm}^{-1}\text{K}^{-1}$. Beyond this, the model becomes increasingly sensitive to the transducer thermal resistance. That is, the thickness and thermal conductivity of the transducer have equivalent sensitivities, so that they are intrinsically paired as a thermal resistance. Thus, to reduce sensitivity to the transducer, one can equivalently increase the thermal conductivity or reduce the thickness of the transducer for the same impact. Practically, the increased sensitivity of $\kappa_{\text{transducer}}$ means higher uncertainty in the measured κ_{sample} , which we find to be overwhelming experimentally above approximately $60 \text{ Wm}^{-1}\text{K}^{-1}$, which is the highest thermal conductivity measured with the present experimental conditions.

To extend the measurement capability of TOPS beyond this limit, we suggest two paths forward. The first is to use the same transducer and increase the laser spot size. Increasing the laser diameter increases the thermal penetration depth into the sample of interest,[1] decreasing the fraction of thermal resistance from the transducer relative to the measurement volume. This effectively increases sensitivity to κ_{sample} relative to $\kappa_{\text{transducer}}$. We can use the same sensitivity analysis to determine the laser diameter at which the sensitivity to κ_{sample} becomes greater

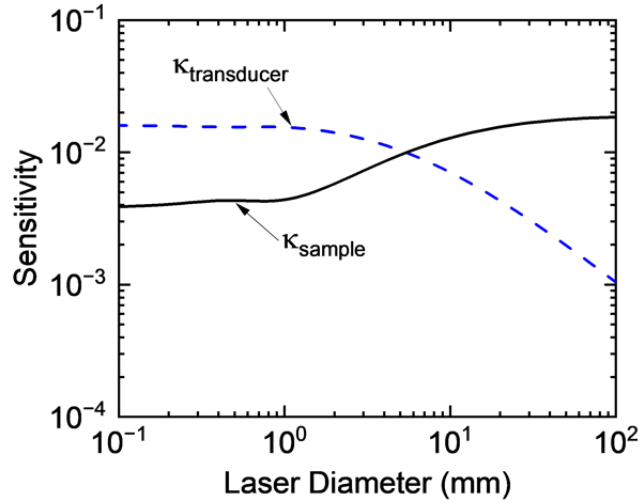


FIG. S5. Sensitivity to thermal conductivity of the sample (κ_{sample}) and the transducer ($\kappa_{\text{transducer}}$) as a function of laser diameter when a standard transducer is used and $\kappa_{\text{sample}} = 100 \text{ Wm}^{-1}\text{K}^{-1}$.

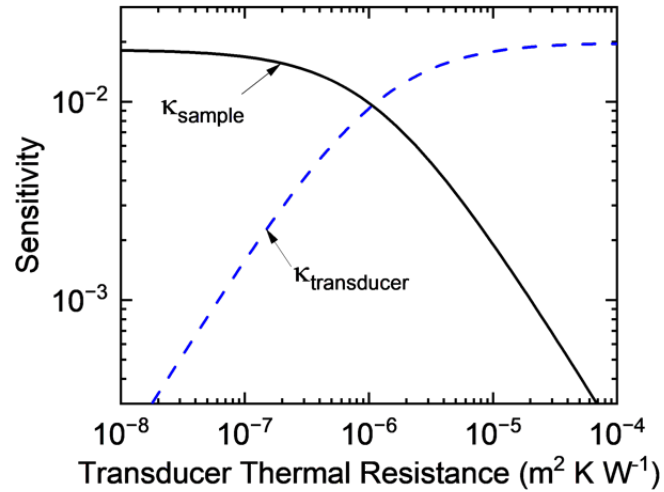


FIG. S6. Sensitivity to thermal conductivity of the sample (κ_{sample}) and the transducer ($\kappa_{\text{transducer}}$) as a function of transducer thermal resistance ($d/\kappa_{\text{transducer}}$).

than $\kappa_{\text{transducer}}$. Let's say we're interested in measuring a sample with maximum $\kappa_{\text{sample}} = 100 \text{ Wm}^{-1}\text{K}^{-1}$. Fig. S5 shows the sensitivity to κ_{sample} and $\kappa_{\text{transducer}}$ as a function of laser diameter to reveal that the sensitivity to κ_{sample} is dominant at a diameter of about 5.5 mm or greater. This suggests that higher thermal conductivity materials can be measured by increasing the spot size. Experimentally, however, there may be limitations in laser power or sample size that restrict this approach in certain situations.

The second method to improving sensitivity to κ_{sample} is to reduce the thermal resistance of the transducer. Again, this can be through reducing the transducer thickness or through increasing the transducer thermal conductivity. To show this concept, we consider a sample having a thermal conductivity of $400 \text{ Wm}^{-1}\text{K}^{-1}$, which barring diamond is the about the highest value one would encounter at room temperature. Figure S6 shows the sensitivity to κ_{sample} and $\kappa_{\text{transducer}}$ as a function of transducer thermal resistance ($d/\kappa_{\text{transducer}}$, where d is the transducer thickness). The transducer thermal resistance needs to be $\leq 1 \times 10^{-6} \text{ m}^2\text{KW}^{-1}$ in order for the sensitivity of κ_{sample} to exceed that of $\kappa_{\text{transducer}}$. Practically, this may be achieved by using a conductive transducer such as graphite, which has at least two orders of magnitude higher thermal conductivity than the polymer we use here. Alternatively, thin film deposition provides a means to deposit films down to nanometers. For example, a 100 nm polymer film ($\kappa = 0.2 \text{ Wm}^{-1}\text{K}^{-1}$) has

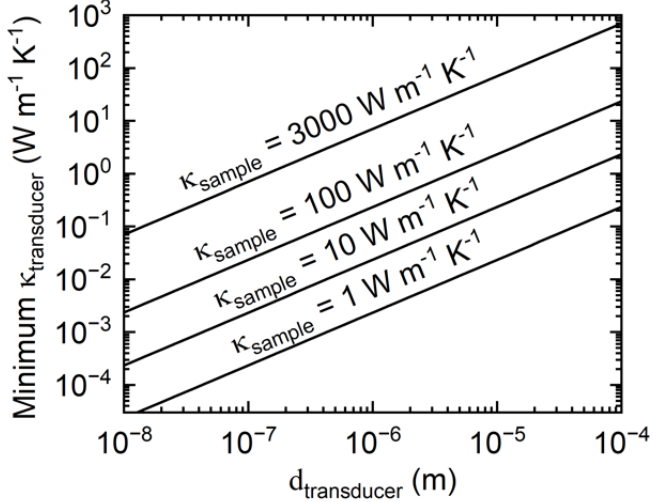


FIG. S7. Minimum transducer thermal conductivity recommended for being able to measure samples having a maximum thermal conductivity of 1, 10, 100, and 3000 $\text{W m}^{-1} \text{K}^{-1}$.

a thermal resistance of $5 \times 10^{-7} \text{ m}^2 \text{KW}^{-1}$, an order of magnitude lower than the aforementioned desired value. Optical opacity to the laser wavelength and IR spectrum of the camera should be considered when choosing the material for this. Metals like titanium, despite poor emissivity, may be good candidates due their optical opacity and ability to be deposited thin and maintain a relatively high thermal conductivity. 200 nm of titanium ($\kappa = 7 \text{ W m}^{-1} \text{K}^{-1}$) would have a thermal resistance of only $2.9 \times 10^{-8} \text{ m}^2 \text{KW}^{-1}$. Figure S7 summarizes the recommended minimum thermal conductivity of the transducer as a function of transducer thickness for various sample thermal conductivities.

IV. UNCERTAINTY ANALYSIS

Uncertainty was calculated using a combination of experimental uncertainty (Δ_{exp}) and model uncertainty (Δ_{model}). Total uncertainty was determined by the $\Delta_{\text{total}} = \sqrt{\Delta_{\text{exp}}^2 + \Delta_{\text{model}}^2}$. Experimental uncertainty was determined using the standard deviation of the five measurements taken on each sample, each at a different location on the sample. This uncertainty proved to be insignificant in almost all samples; the majority of samples had experimental uncertainty less than 1%.

Model uncertainty was determined by first defining the uncertainties of the defined parameters that comprise the thermal model defined in Section I. There were four major sources of uncertainty input into the model: Air conduction, air convection, transducer thermal conductivity, and laser diameter uncertainty. The air thermal conductivity was set to $0.026 \pm 0.001 \text{ W m}^{-1} \text{K}^{-1}$, which should account for any small differences from fluctuations in ambient temperature over time. Air convection was set to $20 \pm 2 \text{ W m}^{-2} \text{K}^{-1}$, based on the ability to capture the low thermal conductivity materials presented in Fig. 4. The transducer thermal conductivity was set to $0.294 \pm 0.02 \text{ W m}^{-1} \text{K}^{-1}$, determined by running TOPS measurements on a 5 mm thick Silicon window with a known κ of $140 \text{ W m}^{-1} \text{K}^{-1}$ and fitting for the transducer κ . Since the silicon has a mirror-finish and such a high thermal conductivity, the overwhelming sensitivity to the thermal model is to the transducer thermal conductivity. In reality, this fitted transducer thermal conductivity and corresponding uncertainty is indicative of the total thermal resistance of the transducer, such that it captures thermal conductivity and thickness, since they are intrinsically paired in the thermal model. Finally, the laser diameter was set to $1.08 \pm 0.03 \text{ mm}$, determined using a camera-based beam profiler (Gentec-EO Beamage-4M). Once defined, the effect of each uncertainty was determined by calculating the relationship $(\Delta T / \Delta P)_{\text{perturbed}}$ when the given input parameter is perturbed by the uncertainty. Since measured κ has a one-to-one relationship with $\Delta T / \Delta P$, we can calculate a $\kappa_{\text{perturbed}}$ that corresponds to the thermal conductivity required to match $(\Delta T / \Delta P)_{\text{perturbed}}$ if only non-perturbed input parameters are assumed. The uncertainty in κ due to input parameter x is then $\Delta_x = |\kappa - \kappa_{\text{perturbed}}| / \kappa_{\text{perturbed}}$. This procedure is repeated for each input parameter in both the + and - directions of uncertainty (which does lose symmetry at the extremes in κ) and combined using $\Delta_{\text{model}} = \sqrt{\sum_x \Delta_x^2}$.

Figure S8 shows the corresponding model uncertainty for the standard configuration coming from (a) air conduction,

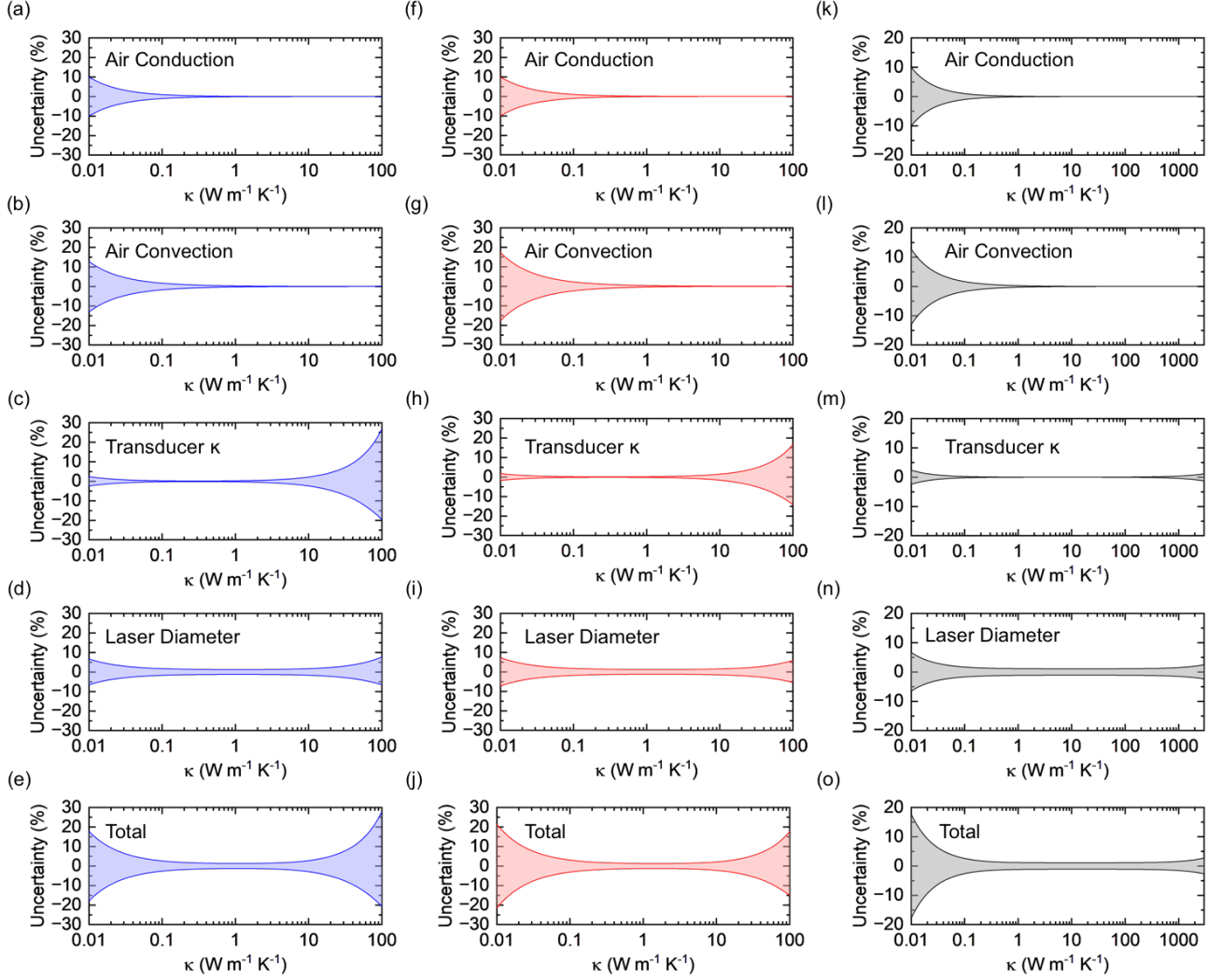


FIG. S8. Model uncertainty as a function of thermal conductivity for three experimental configurations: (a-e) the standard configuration used in this study using a 1.08 mm diameter laser and the 5 micron polymer-based transducer, (f-j) using a 2.16 mm diameter laser (2× the standard configuration) and same transducer, and (k-o) Using the 1.08 mm diameter laser but now modeling a 200 nm Ti transducer. The model uncertainties shown are further broken down based on individual contributions from each parameter: (a,f,k) air conduction, (b,g,l) air convection, (c,h,m) transducer κ , (d,i,n) laser diameter, and (e,j,o) total uncertainty from combining these individual components.

(b) air convection, (c) transducer κ , (d) laser diameter, and (e) total uncertainty. On the low end of the thermal conductivity spectrum, it is clear that air conduction and convection contribute most to total uncertainty, since the thermal resistance of the air becomes less than the sample itself below $0.026 \text{ Wm}^{-1}\text{K}^{-1}$. On the high end of the spectrum, the transducer is the major source of uncertainty, due to the transducer thermal resistance dominating the thermal response to laser heating. Finally, laser diameter has a relatively strong impact on total uncertainty towards both the low and high ends of thermal conductivity, but is minor between $0.1 - 10 \text{ Wm}^{-1}\text{K}^{-1}$. In the standard configuration model uncertainty is <5% for κ ranging from $0.04 - 20 \text{ Wm}^{-1}\text{K}^{-1}$ and <10% uncertainty for κ ranging from $0.018 - 40 \text{ Wm}^{-1}\text{K}^{-1}$. Total uncertainty demonstrates the practical limits to measurement. Much like the conclusion of the sensitivity analysis above, the uncertainty analysis shows us that measuring high thermal conductivity materials has a fundamental challenge that limits measurement accuracy: the transducer is too thermally resistive, so any uncertainty gets propagated significantly when measuring high- κ materials.

It is instructive to consider two additional experimental conditions discussed in Section III; in that discussion we suggested two paths towards extending the TOPS measurement range to higher thermal conductivities: increasing the beam size and using a less thermally resistive transducer. We consider both scenarios here, summarized in Table S1.

First, we consider doubling the laser diameter. Figure S8(f)-(j) show the resulting uncertainties coming again from (f) air conduction, (g) air convection, (h) transducer κ , (i) laser diameter, and (j) total uncertainty. The doubling of the laser diameter decreases the overall uncertainty at the high end of the κ range, but increases uncertainty at the low end, leading to a <5% uncertainty window for κ ranging from about $0.05 - 28 \text{ W m}^{-1}\text{K}^{-1}$ and <10% uncertainty for κ ranging from $0.023 - 62 \text{ W m}^{-1}\text{K}^{-1}$. Finally, we consider the use of a 200 nm Ti transducer instead of the standard transducer used. In addition to having a $25\times$ reduction in thickness, it has a $24\times$ higher thermal conductivity, leading to a $600\times$ reduction in thermal resistance. Figure S8(k)-(o) show the resulting uncertainties coming again from (k) air conduction, (l) air convection, (m) transducer κ , (n) laser diameter, and (o) total uncertainty. It is clear from the total uncertainty that high thermal conductivity samples, even diamond, become measurable in theory. Of course, there may be experimental challenges involved in conducting such measurements that are not captured in modeling alone. Moreover, there are practical limitations of using a thin metal transducer; in addition to requiring a tool to deposit, it is not applicable to many materials, including liquids and porous samples. Additionally, the sample surface roughness requirements will likely be more strict than in the case of the standard configuration transducer. Nonetheless, this analysis is motivating for extending the measurement range of TOPS in future iterations.

TABLE S1. Uncertainty of model parameters under different configurations.

Uncertainty Name	Model Parameter	Standard Configuration	2x Laser Diameter	200 nm Titanium Transducer
Air Conduction	κ_{air}	0.026 ± 0.01	0.026 ± 0.01	0.026 ± 0.01
Air Convection	H	20 ± 2	20 ± 2	20 ± 2
Transducer	$\kappa_{\text{transducer}}$	0.294 ± 0.020	0.294 ± 0.020	7 ± 0.5
Laser Diameter	$2r_0$	1.08 ± 0.03	2.16 ± 0.06	1.08 ± 0.03

-
- [1] Jeffrey L. Braun and Patrick E. Hopkins. Upper limit to the thermal penetration depth during modulated heating of multilayer thin films with pulsed and continuous wave lasers: A numerical study. *Journal of Applied Physics*, 121(17):175107, 2017.
- [2] Jeffrey L. Braun, David H. Olson, John T. Gaskins, and Patrick E. Hopkins. A steady-state thermoreflectance method to measure thermal conductivity. *Review of Scientific Instruments*, 90(2):024905, 2019.